POLITECNICO
MILANO 1863

SCUOLA DI INGEGNERIA INDUSTRIALE
E DELL'INFORMAZIONE

A Comprehensive Model for the Thermal Plasma Conversion of Methane to Hydrogen and Carbon

MASTER THESIS IN
CHEMICAL ENGINEERING

Author: **Alberto Cadenelli**

Student ID: 970571
Advisor: Carlo Alessandro Cavallotti
Academic Year: 2021-22

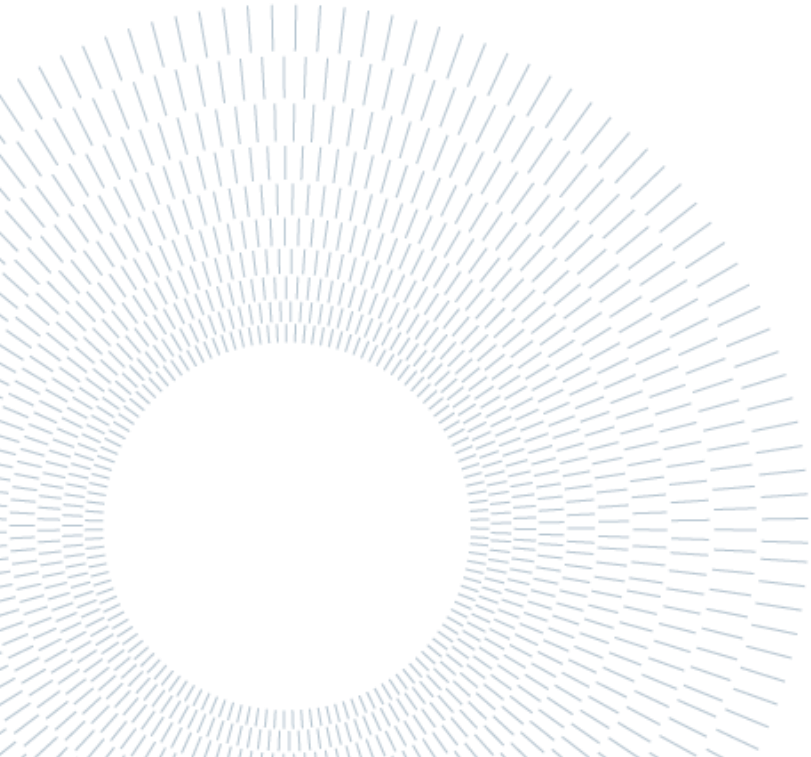

Abstract

The use of fossil fuels for heating and transport is among the main causes of climate change. The most impacting byproducts of fossil fuels combustion are the NO_x and CO_x. Therefore the European Union has developed a detailed plan for decarbonizing the transport, industry, and heating sectors. The hydrogen production has a key role in the European plans. The usual processes to obtain it from fossil fuels are not environmentally friendly, while the more sustainable methods, such as those exploiting electrolysers, are not so convenient from an energetic and economical point of view. A promising strategy can be the use of dedicated catalysts to make such processes more economical sustainable. But also the use of plasma can be a possible way to produce hydrogen, with the advantage to use a largely available resource (methane) and not to produce directly carbon dioxide.

The aim of this thesis if to investigate in detail the operative conditions that allow to maximize hydrogen production. The chosen approach consists of three steps.

The first is to develop a model to describe what happens inside the plasma discharge. This model is functional to understand which temperatures are reached in the discharge and the main features of the plasma discharge.

The second step is represented by the definition of the composition of the gaseous mixture exiting the plasma discharge. Here the attention will focus on the species that are formed in different conditions and on which settings allow to maximize the solid formation to reduce the production of acetylene, which is considered a byproduct.

The third stage will be dedicated to the reaction system after the plasma arc section. It is in this case of key relevance to establish in which conditions the formation of the carbon particulate can be triggered. The main parameters that seem to affect the gas phase carbon formation are the reactor diameter (thus the residence time) and the temperature profile in the cooling zone.

Key-words: thermal plasma, hydrogen, soot formation.

Abstract in italiano

L'uso di combustibili fossili per il riscaldamento e il trasporto è tra le principali cause del cambiamento climatico. I sottoprodotti più impattanti della combustione di combustibili fossili sono NOx e COx. Pertanto, l'Unione Europea ha sviluppato un piano dettagliato per la decarbonizzazione dei settori dei trasporti, dell'industria e del riscaldamento. La produzione di idrogeno ha un ruolo chiave nei piani europei. I processi usuali per ottenerlo da combustibili fossili non sono ecologici, mentre i metodi più sostenibili, come quelli che sfruttano gli elettrolizzatori, non sono così convenienti dal punto di vista energetico ed economico. Una strategia promettente può essere l'uso di catalizzatori dedicati per rendere tali processi più economicamente sostenibili. Ma anche l'utilizzo del plasma può essere una possibile via per produrre idrogeno, con il vantaggio di utilizzare una risorsa largamente reperibile (il metano) e di non produrre direttamente anidride carbonica.

Lo scopo di questa tesi è quello di indagare in dettaglio le condizioni operative che consentono di massimizzare la produzione di idrogeno. L'approccio scelto si compone di tre fasi.

Il primo è sviluppare un modello per descrivere cosa accade all'interno della scarica di plasma. Questo modello è funzionale per capire quali temperature vengono raggiunte nella scarica e le caratteristiche principali della scarica del plasma.

Il secondo step è rappresentato dalla definizione della composizione della miscela gassosa in uscita dalla scarica di plasma. Qui l'attenzione si concentrerà sulle specie che si formano nelle diverse condizioni e su quali impostazioni consentono di massimizzare la formazione di specie solide per ridurre la produzione di acetilene che è considerato un sottoprodotto.

La terza fase sarà dedicata al sistema di reazione dopo la sezione dell'arco plasma. È in questo caso di fondamentale importanza stabilire in quali condizioni può essere innescata la formazione del particolato di carbonio. I parametri principali che sembrano influenzare la formazione di fuliggine sono il diametro del reattore

(quindi il tempo di permanenza) e il profilo di temperatura nella zona di raffreddamento.

Parole chiave: plasma termico, idrogeno, formazione di particolato.

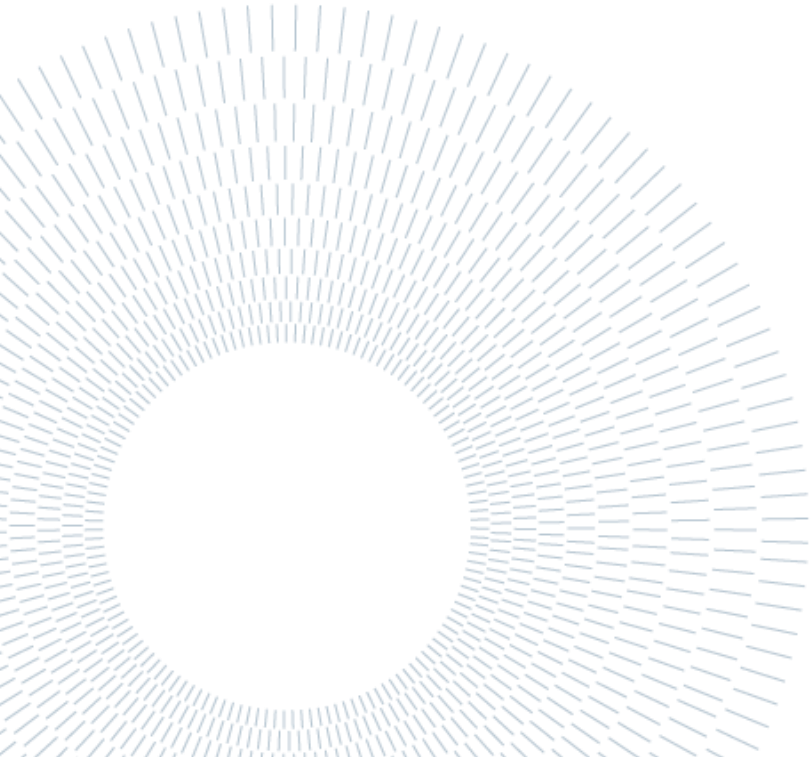

Contents

Abstract ..... **i**

Abstract in italiano ..... **iii**

Contents ..... **vii**

1 Introduction and state of the art **1**

European Hydrogen Strategy 1

1.1. Hydrogen production 6

1.1.1. Hydrogen production from fossil fuels 9

1.1.2. Water electrolysis 10

1.1.3. Hydrogen production by solar energy 11

1.1.4. Water electrolysis by wind energy 16

1.1.5. Hydrogen production from biomass 17

1.1.6. Biological hydrogen production processes 18

1.1.7. Purple hydrogen production method 21

1.2. State of the art in hydrogen production by using plasma 23

1.3. Conclusions and aim of the thesis 33

2 Methods **35**

Plasma discharge model 35

2.1.1. The Steenbeck-Raizer Model of the thermal arc discharge 35

2.1.2. Alternative models of plasma arcs 40

2.2. Plasma thermodynamic model 42

2.2.1. Plasma thermodynamic model, only gaseous phase 42

2.2.2. Plasma thermodynamic model with solid formation 44

2.3. System reactivity after plasma-bypass mixing 46

3 Results **51**

3.1. Results of Raizer-Steenbeck model of a plasma discharge 51

3.2. Results of an alternative model of a plasma discharge 61
3.3. Results of the thermodynamic model 63
3.3.1. Results of the thermodynamic model (only gaseous phase) 63
3.3.2. Results of the thermodynamics model (also considering the solid phase) 69
3.4. Results derived from OpenSMOKE++ suite simulations 75
4 Conclusion and future developments 84
Bibliography 85
List of Figures 93
List of Tables 97
Acknowledgments 101

1 Introduction and state of the art

In this section the hydrogen energy production sector is reviewed, and the aim of the thesis defined. The emphasis is initially placed on strategic aspects at the European political and technological level. A survey on the different technological approaches to hydrogen production is then reported (section 1.1), after which plasma systems for hydrogen production are introduced and discussed (section 1.2). The aim of the thesis is defined in section 1.3.

European Hydrogen Strategy

The 2022 Intergovernmental Panel on Climate Change (IPCC) report [1] on the impacts, adaptation and vulnerability has pointed out the need to drastically reduce global emissions. Greenhouse gases (GHGs) emissions must be reduced by at least 45% by 2030, and carbon neutrality must be reached by 2050 to stay below the rise of 1.5 ◦C with respect to the pre-industrial age [2].

The average GHG emissions during 2010-2019 were the maximum in the last century, but the growth rate was lower than during 2000-2009.

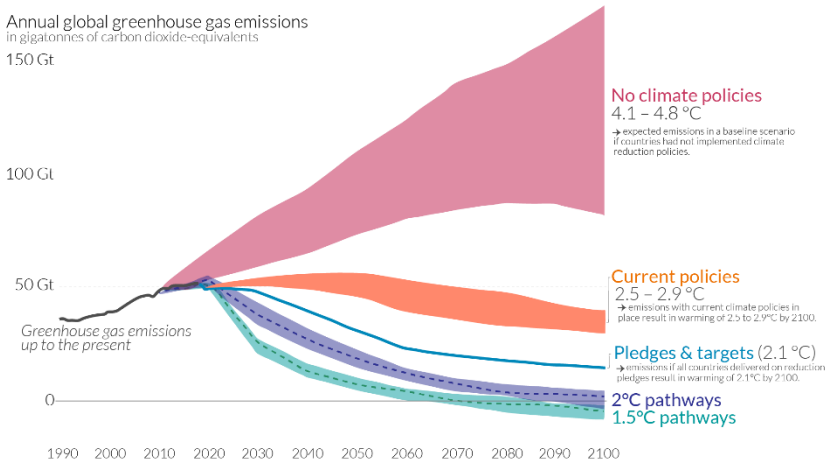

Figure 1.0.1: Global GHG Emissions and warming scenarios. Source: Our World in Data [3].

Mean and maximum temperatures have increased since 1950. According to the projections, if countries do not implement a climate mitigation plan, the temperature rise at the end of the century will be equal to 5°C [4]. While if they implement the current policies, the temperature increment would be in a range around the 2.75°C. These trends are reported in Fig 1.0.1.

On 14th July 2021, the European Commission presented the Fit for 55 plan. This plan is extremely ambitious since the proposed goal is a greenhouse gas emissions reduction of 55% by 2030 thanks to a series of legislative proposals about energy and environment to renew the industrial and transportation sectors. The package aims are:

- Guarantee a socially equal transition
- Maintains the innovation and competitiveness of EU industrial sector in spite of the huge transition costs
- Make European Union the leader in the climate change fight

In 2022, when Russian Federation has attacked militarily Ukraine, the EU's over-dependence on gas, oil, and coal imports from Russia has manifested itself showing the weakness of the current EU energy system. In the figure 1.0.2 the relative dependance of European countries from Russian gas is depicted.

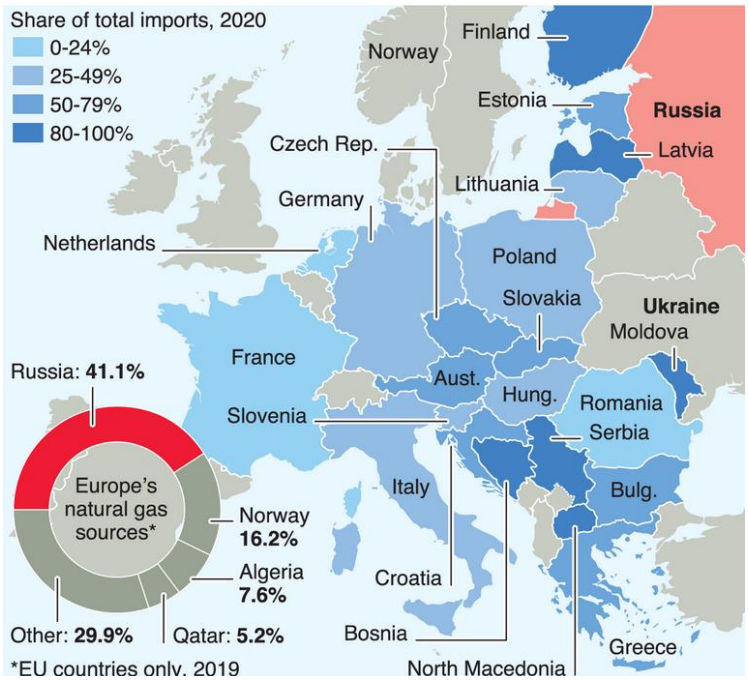

Figure 1.0.2: European countries dependance on gas from the Russian Federation. Source Eurostat, Bloomberg, and Statista [5].

In March 2022, EU leaders decided in the European Council that it was time to become independent from Russian energy imports as soon as possible.

REPowerEU [7] is a detailed program to reduce European dependence as rapidly as possible on Russian fossil fuels, especially from the natural gas, by accelerating the sustainable transition and building a more resilient and independent energy system from extra-UE countries.

This REPowerEU plan puts forward an additional set of actions to (Fig 1.0.3.):

- save energy improving the efficiency of the current energy systems;
- diversify supplies, to not be excessively dependent from a unique country;
- quickly substitute fossil fuels for accelerating the European energy transition, with different energy carriers as hydrogen or biofuels in order to abate CO_2 emissions;
- efficiently combine investments and reforms for the energy and environment sector, especially for the research

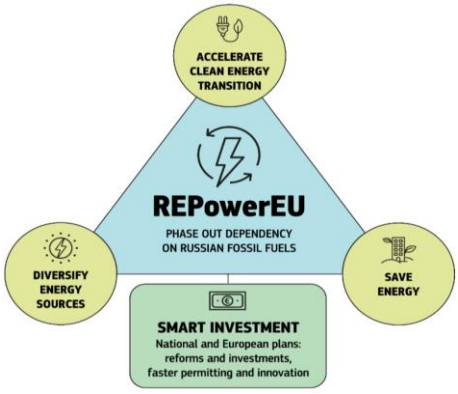

Figure 1.0.3: Three main programmatic points of REPowerEU plan [7].

REPowerEU [7] is built on the full implementation of the Fit for 55 proposals maintaining the ambition of achieving at least -55 % net GHG emissions by 2030 and climate neutrality by 2050 in line with the European Green Deal.

The reduction of dependance of Russian fuels requires to reduce the use of fossil fuels and diversify the gas supplies, improving the LNG imports and pipelines from non-Russian countries, and also with higher biomethane production. The Fit-for-55 plan proposed to reduce EU gas consumption by 30% (116 bcm) by 2030, while REPowerEU [8] planned to reduce or diversify at least 155 bcm of natural gas, i.e. the equivalent of imports of Russian gas by 2027.

REPowerEU [8] plan considered three different time horizons, short-term, medium-term, and long-term.

The development of renewable hydrogen and its relative infrastructure belongs to the long-term horizon. The European Commission has proposed in the previous plan a minimum production of renewable hydrogen for industrial sectors, but in order to break off the Russian dependance the EU needs to accelerate the renewable hydrogen production by 2030: the plan consists of producing 20 Mt of green hydrogen, about four times the previous goal (5,6 Mt) [8].

It has been considered the idea of blending hydrogen into the natural gas grid. The blending leads a series of consequences that must be evaluated. The overall system and adaptation costs for final users are considerably high, blending a 5% of hydrogen with NG leads to spend € 3.6 billion per year.

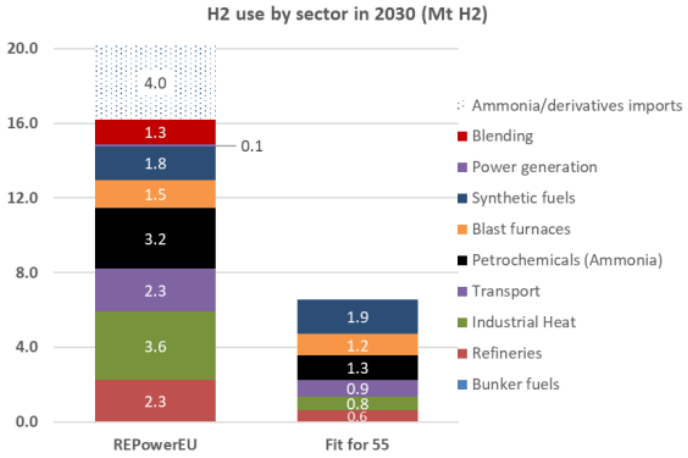

Figure 1.0.4: Hydrogen use by sector in 2030 (Mt H2); Source: Modelling using PRIMES [7].

Hydrogen production is one of the key point contained in commission proposals, especially as alternative fuel for transportation sector and for hard-to-abate industrial sectors, sector where the transition technology lack, or its cost remains prohibitive. The hydrogen application sectors are summarized for the two different European commission plans in Fig 1.0.4.

Hydrogen has several advantages, it is one of the highest energy density fuels, is environmentally friendly, and can be produced in different sustainable ways.

Currently, hydrogen can be produced from a wide variety of resource such natural gas, coal, biomass, water; metal hydrides, H2S, and biological sources such as biomass.

Nowadays, hydrogen is used mainly in oil refining and production of ammonia, but it has not yet found a diffuse utilization in transportation and power generation, however, it is expected to grow in these sectors in future for fight the climate change.

In the following paragraph the different hydrogen production methods will be analyzed. Before doing that it is though convenient, to give a clear prospective of the hydrogen sector, to discuss briefly, the problems related to hydrogen storage [9].

With the massive diffusion of renewable energy, which has an intermittent character, the interest in energy storage technologies has exponentially increased in the industrial sector. Hydrogen, by the use of fuel cells, represents a very promising energy storage medium since it is a flawless energy carrier. But hydrogen storage has a density problem: 1 kg of hydrogen occupies one cubic meter under normal pressure and temperature. The problem can be avoided using pressurized vessels or liquefaction, leading at higher management costs.

The most diffused storage methods are the physical ones [10]: liquid tanks, compressed tanks and the combination of the previous methods, the cryo-compressed tanks. These solutions, especially the compressed tanks, present some drawbacks regarding the safeness of plants and people living nearby and the overall maintenance costs.

As a consequence, the research has directed its focus on a different strategy, i.e. chemical storage. The chemical storage can be distinguished in three macro-categories: chemical hydrides, metal hydrides and sorbents [10].

In chemical hydrides means hydrogen is bonded chemically. They usually exist in liquid form at standard conditions. Examples of this category include ammonia and methanol.

Metal hydrides are compounds where metal atoms form strong chemical bonds with hydrogen. These bonds cannot be broken easily, as a high energy input is required. In normal conditions, these hydrides have a significant storage density. Hydrogen can be recovered by hydrolysis or thermolysis.

Hydrogen adsorbs on a substance with a big specific surface area thanks to van der Waals bonds. The process occurs at a pressure between 10 and 100 bar. The absorbents for hydrogen can have different nature: porous carbon-based materials, metal-organic frameworks, and zeolites. Since low densities of the adsorbent and cost affective optimization the greater storage density that can be reached is 40-50 kg/m^3.

1.1. Hydrogen production

The conventional production routes, which principally comes from fossil fuel, have negative environmental impacts. Therefore, renewable sources are considered optimal solutions for a sustainable production of hydrogen.

A list of the most used energy sources is reported in Fig.1.1.1. They can belong to different type such as nuclear, wind, biomass, hydro and solar [11].

The different energy sources can be used to get different type of energy: radiation, thermal, electrical, biochemical, and photonic energy. Each of these energy sources can be declined in several hydrogen production processes [11]. For instance, biochemical energy can be utilized into enzymatic process, fermentation, or metabolic process.

Besides the different energy sources can be combined together to achieve the hydrogen production, for example the solar and biochemical energy can be combined in the photochemical process.

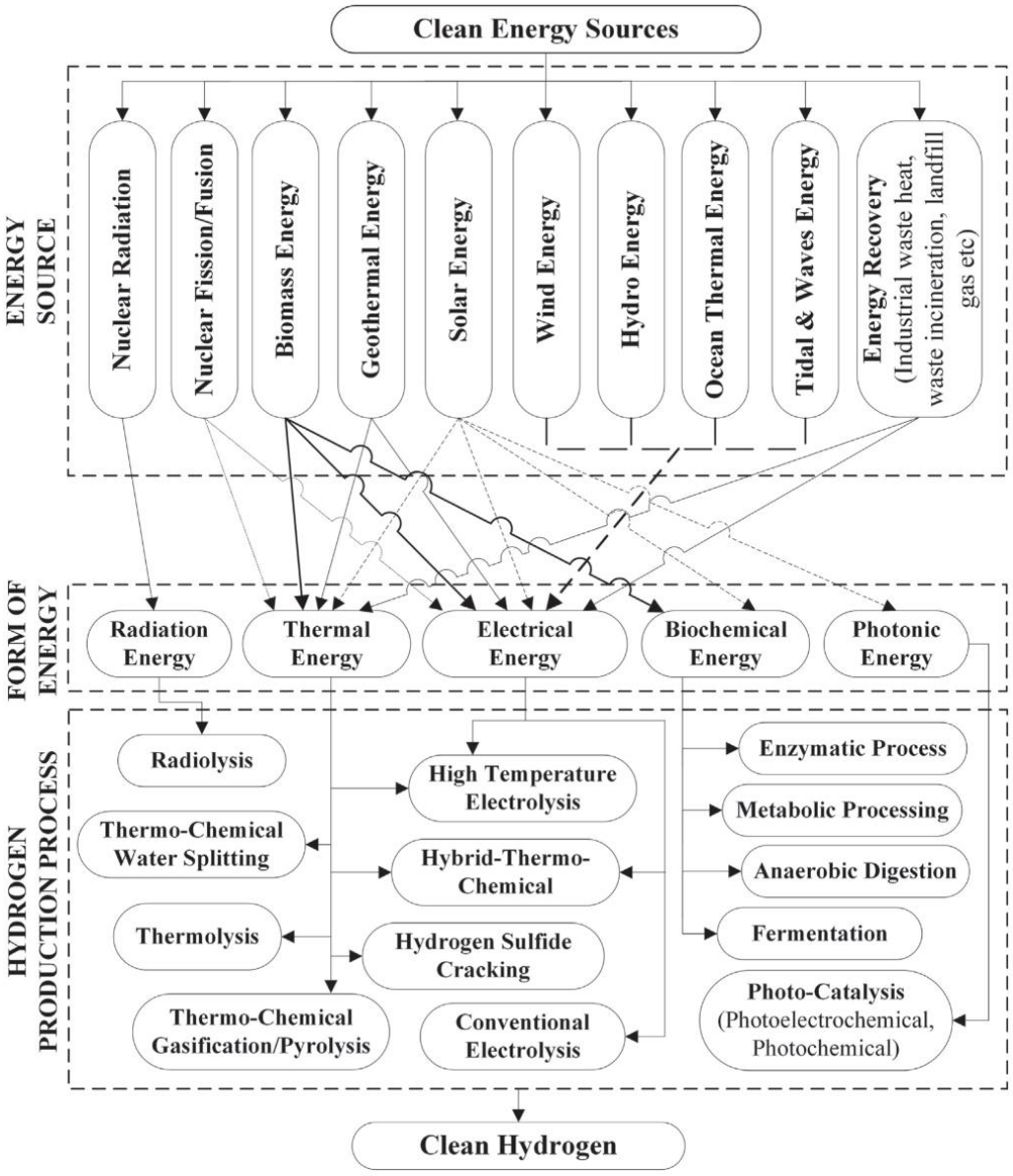

Figure 1.1.1: Routes for sustainable clean hydrogen production. [11]

The cost of hydrogen extremely depends on energy source used for the production. But also the cost of energy source varies depends significantly on the country where it is produced. In Figure 1.1.2 the cost ranges for hydrogen production are reported. It is interesting to underline how the range for the cost relative to solar hydrogen is very wide. The reasons of a so wide range are correlated at the different existing technology.

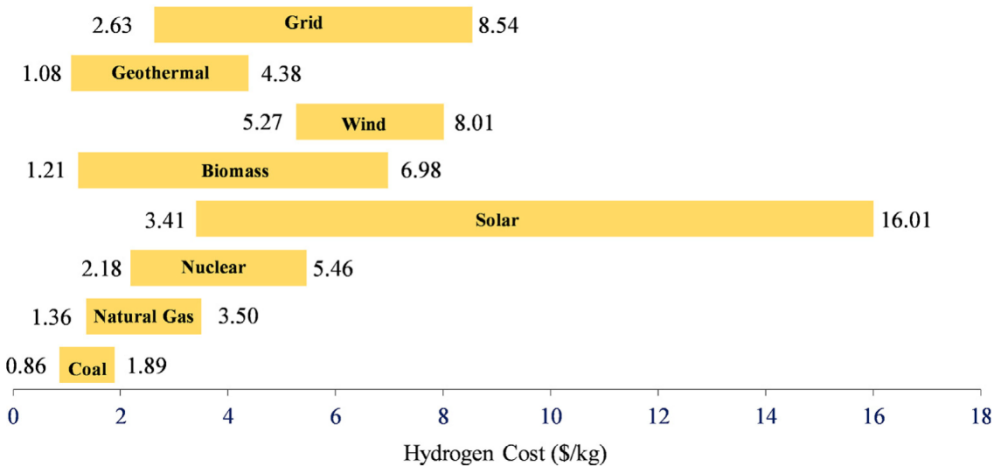

Figure 1.1.2: Cost range of hydrogen production technologies based on energy source. [11]

Hydrogen production must include actions to ensure safe production and storage, since it is a highly active gas, which may increase the production cost. For example, H2 storage containers and transportation pipelines require high pressures to ensure no leakages.

In Figure 1.1.3 the production costs for hydrogen [10] are reported for each type of source both renewable and fossil fuels. From the graph it is deduced that the classical method for hydrogen production are already competitive with respect to the green and clean method.

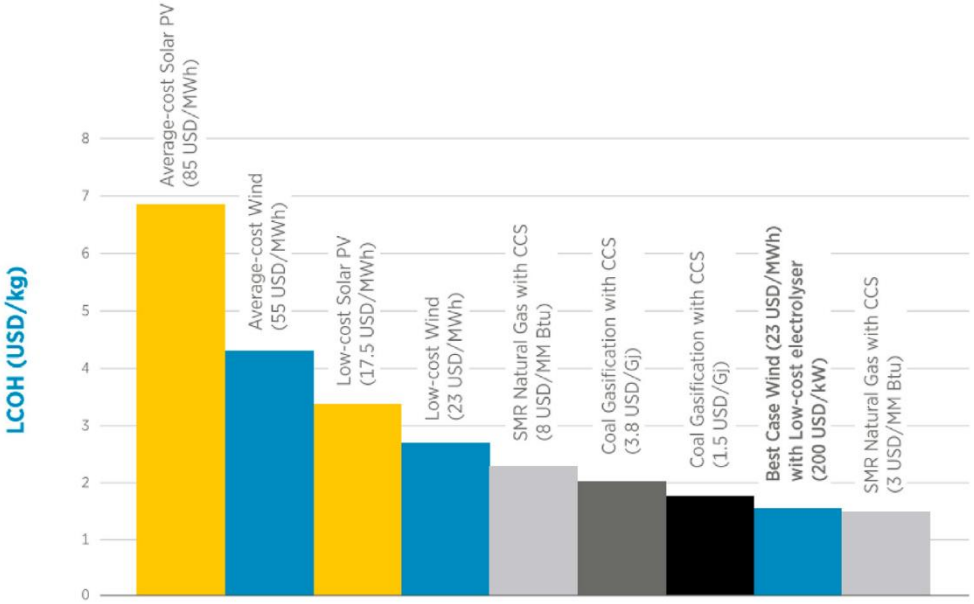

Figure 1.1.3: Hydrogen production cost by renewable and non-renewable energies in 2019 [10]

1.1.1. Hydrogen production from fossil fuels

Methane Steam Reforming (MSR) is the most diffused method for producing hydrogen from natural gas [12].

Before the reforming process, methane is desulfurized (sulfur impurities are removed in order to avoid catalyst poisoning). In MSR, the natural gas and steam react at 700–1000 °C under a pressure range of 3–25 bar over a catalyst, where an hydrogen and carbon monoxide mixture, i.e.,. syngas, is produced. Ni/Al2O3 is the most used commercial catalyst for MSR.

The reforming is followed by a shift converter, where extra H2 is produced from CO by steam addition. Subsequently, a pressure swing adsorption is used to remove the CO2 gases getting pure H2 as an outcome of the process.

This process efficiency is of 65-75% and can reach more than 80% for large reformers. Also, it is considered as the most economical method. The following equation shows the chemical reaction of MSR:

$$CH_4 + H_2O \rightarrow CO + 3H_2$$

Intensification of the methane steam reforming process plays a key role, in order to achieve the objectives, set by the EU regulation. The process electrification could become competitive only if the electricity used comes from renewable energy sources. The methane used in the MSR is mainly of fossil origin, however also the bio-methane generated by the anaerobic digestion can be used.

Coal gasification is also used for hydrogen production [13]. In the coal gasification process, coal is partially oxidized with oxygen and/or steam under high pressure and temperature. Carbon monoxide (CO) and H2 are the main products of this partial oxidation. A shift reaction is used to increase hydrogen yield. The high carbon content of coal leads to produce substantial amounts of CO2 compared to other feedstocks, this is the major drawback of coal gasification. A Carbon Capture and Storage (CCS) technologies can be coupled for minimizing undesired CO2 emissions during coal gasification.

Glycerol Steam Reforming [12] contemplate the use of glycerol in a reforming processes. This process is very promising since it could theoretically provide seven moles of hydrogen for every mole of C3H8O3.

Moreover glycerol is a by-product of biodiesel production obtained in large amount. The use of glycerol for the production of high value chemical, as hydrogen, appears to be a promising way to exploit its potentiality and simultaneously increase the global biodiesel market.

In the case of glycerol steam reforming, the noble metal-based catalysts show excellent performance, in particular with Pt-based catalysts, moreover the presence of promoters suppresses the coke formation, however the inflated cost makes them uncompetitive compared to nickel-based catalysts.

Nano-sized Ni-based steam reforming catalysts for glycerol are produced successfully starting from LaNiO3 and CeNiO3 as base materials by varying the formulation, mixing them, or incorporating varying amounts of ZrO2 o SrO.

1.1.2. Water electrolysis

Water electrolysis is a process [10, 13] through which water is split into hydrogen and oxygen by adding electricity, as described in the following equation.

$$H_2O \rightarrow \frac{1}{2}\, O_2 + H_2$$

Water electrolysis is considered to be the cleanest method for producing hydrogen since no carbon emissions are generated, but unfortunately, the water dissociation requires a significant amount of energy ($\Delta H0$ = 285.8 kJ·mol^{-1} and $\Delta G0$ = 237.2 kJ·mol^{-1} under standard conditions).

The principle limitation is the slow kinetics, so that in order to reach a significant hydrogen production rate, cell voltages of 1.8–2.0 V are required, thus increasing the costs, and decreasing the efficiency of the process.

Many electrolyser types are available, such as proton exchange membrane (PEM), alkaline, and solid oxide electrolysers. After the electrolyser, a compressor is usually used to store hydrogen. The scheme in Fig. 1.1.4 summarizes the steps for hydrogen production and storage by water electrolysis.

The source of input power can be renewable energy, making the full process even more sustainable.

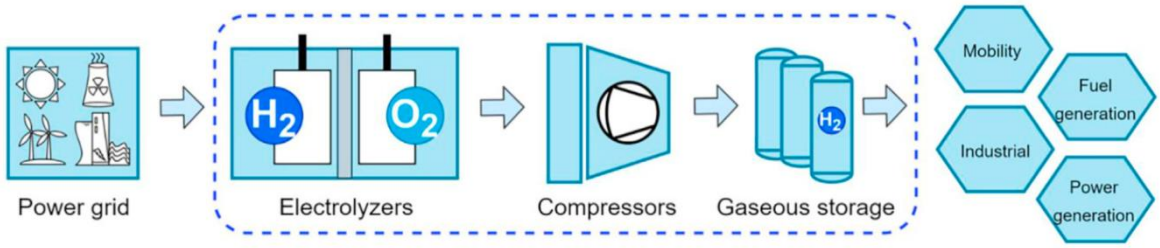

Figure 1.1.4: Scheme of hydrogen production by electrolyser [10]

1.1.3. Hydrogen production by solar energy

The solar energy source can be subdivided into four categories, the solar thermal, solar photovoltaic, photo-electrochemical, and photocatalytic classes.

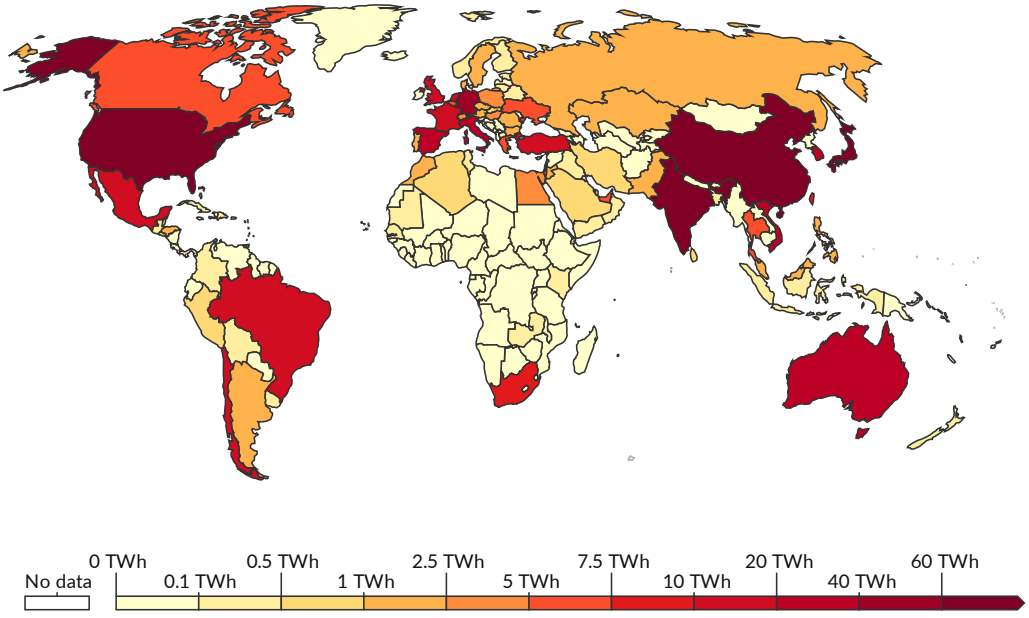

Figure 1.1.5: Solar power generation, 2021, electricity generation from solar, measured in TWh per year. Source: Our World in Data [14]

The solar energy production is one of the most diffused renewable resource since the technology costs in the last decade is significantly decreased. In Fig 1.1.5 the global energy production by solar power measured in TWh per year.

1.1.3.1. Hydrogen production by thermal solar energy

Solar concentrating power plants [15] can be managed to produce hydrogen, this process is one of the best methods for hydrogen production through a thermochemical process. Such a method has high efficiency and does not require precious catalysts, which could be damaged during the hydrogen production.

The process consists of use of mirrors and parabolic dishes to focus the incident solar energy on a smaller area. Also some power towers can be used to increase the available temperature that can be for hydrogen production.

Thermochemical processes include also reforming, gasification, cracking, and water thermolysis/ thermal splitting. The most sustainable method among them is water thermolysis [9], and hence it is the most diffused one. The main challenges concerning its wide adaptation are the extremely high operational temperatures in a range between 2500 K and 3000 K, limiting the materials that can resist at these elevated temperatures and be at a reasonable and sustainable cost. In addition, it is required a separation system to avoid the recombination of hydrogen and oxygen.

A competitive alternative is to use Concentrating Solar Power (CSP) [15] to first generate electrical power, which can be subsequently used in an electrolysis plant. The two-step thermochemical cycles offer two major advantages respect with the direct solar thermolysis, the scheme is reported in Fig 1.1.6:

1- The gas separation occurs by absorption of oxygen into reactor material, usually mixed-metal ferrite, while hydrogen is simply released.
2- The required temperature is ridiculously lower than in thermolysis.

It must also consider that this type of system can reach a theoretical efficiency up to 70%.

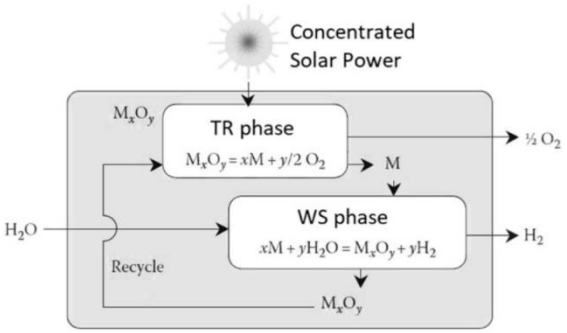

Figure 1.1.6: Two stages of the water-splitting process [15]

The first reaction is a endothermic thermal reduction reaction (TR), where the metal oxide is reduced, removing a part of oxygen. The second step provides the exothermic water splitting (WS).

1.1.3.2. Water electrolysis by Photovoltaic solar energy

Solar power is abundant, available and a sustainable source of energy. However, the efficiency of photovoltaic solar cells reaches 10-20% of incident power depending on several parameters such as dust on cells surface, operating temperatures, and constitutive cells materials.

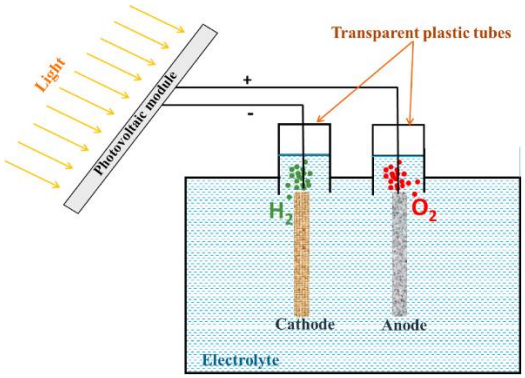

Figure 1.1.7: Hydrogen production by solar PV system. [10]

Therefore, for solar PV to supply the entire required electrical demand is challenging. Additionally, solar power has limited availability as it is only available during daytime. Such limitation could be reduced or eliminated through the use of hybrid systems consisting of other renewable energy sources and/or storage systems.

An electrical power produced by solar PV modules could be used to produce hydrogen through an electrolyser [10]. The schematic in Fig.1.1.7 shows the coupling of a solar PV system and water electrolyser used for hydrogen production.

Having a PV system with higher efficiency will produce higher energy for the same module area, and hydrogen production will also increase. This coupling is considered as one of the most sustainable systems for hydrogen production.

The disadvantages of producing hydrogen by PV system are the high installation costs and the lower exoergic performance compared to fossil fuel. However, PV production costs are in a steady decline with a lower cost per kWh. The system can

be coupled with other energy resources to maximize efficiency and allow hydrogen production also to nighttime.

1.1.3.3. Water splitting by photoelectrochemical methods

Photoelectrochemical cells (PEC) [16] can convert solar energy to an energy carrier by light stimulated electro chemical processes. The photoelectrodes absorbs solar light, at least one of them is a semiconductor [12]. Three different scheme for the preparation of the water splitting system can be explored: single photo-anode or -cathode or the tandem system of the two previous solutions (Figure 1.1.8).

PECS can produce either chemical or electrical energy, so that it is possible to produce directly or indirectly hydrogen. The working principle of PECs is similar to PV cell: photons with higher energy than the band gap generate electron-hole pairs and this electric fields allow to reduce or oxidize water.

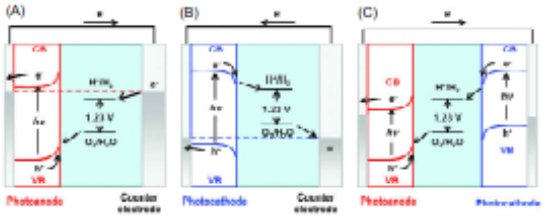

Figure 1.1.8: Three different configurations for PEC water splitting system are explored, single photoanode, single photo-cathode, photoanode and photocathode tandem system. [16]

PEC units are more compact than PV cell and its relative electrolyser since PEC combines the energy absorption and water electrolysis into a single unit. In the literature the most promising option is agree to be TiO_2. In addition to titania, several different semiconductors have been studied such as, F_2O_3, $BiVO_4$ and Ta_3N_5 [12].

1.1.3.4. Hydrogen production by photocatalytic methods

The photocatalysis [16] is a process which converts photon energy to chemical energy leading to the hydrogen production. The energy carried is correlated to the frequency of the radiation, and this aspect represents one of most concerning challenges since the system is projected to be implemented with visible light use, whose photon conversion efficiency is low.

$$H_2O \xrightarrow{hv\ on\ photocatalyst} \frac{1}{2}\ O_2 + \ H_2$$

The feasible photocatalysts must meet some fundamental properties to achieve a reasonable efficiency to provide the photocatalytic water splitting. The most significant properties to consider a material as a good photocatalysts are [12]:

- Capability to absorb visible light
- Chemical stability under redox conditions
- Low cost and high recyclability
- Performant chemical resistance
- Adaptability for large-scale hydrogen

TiO_2 is the benchmark photocatalyst for hydrogen production despite a low light absorption when the wavelength is higher than 350 nm (visible light spectrum).

An available strategy for improving the absorption is doping the titania with a suitable element, the scheme of change is represented in Fig. 1.1.9. The dopant acts as promoter reducing the reaction rate, a feasible choice consists of N atoms in spite of N dopant is difficult to solve into the titania [17].

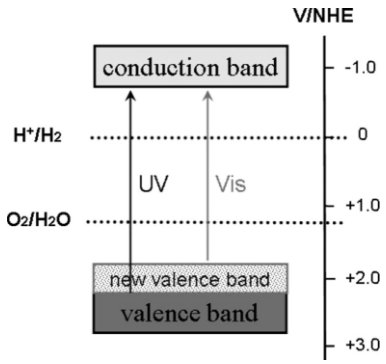

Figure 1.1.9: New valence band formation by doping of nonmetal ions. [17]

Nitrogen substitutes the dioxygen ions in the photocatalyst lattica create a new state above the valence band. This state allows the enhancement of light absorption because the gap betweem the conduction and new valence band is reduced enough that the energy carried by the visible light can provide the photocatalysis for hydrogen production.

1.1.4. Water electrolysis by wind energy

For generating electricity wind turbines are used to extract wind energy [8]. The wind rotates the turbines which convert kinetic energy into mechanical energy and the generator converts mechanical energy into electrical energy. In Fig 1.1.10 the global wind power generation is shown and measured in TWh per year.

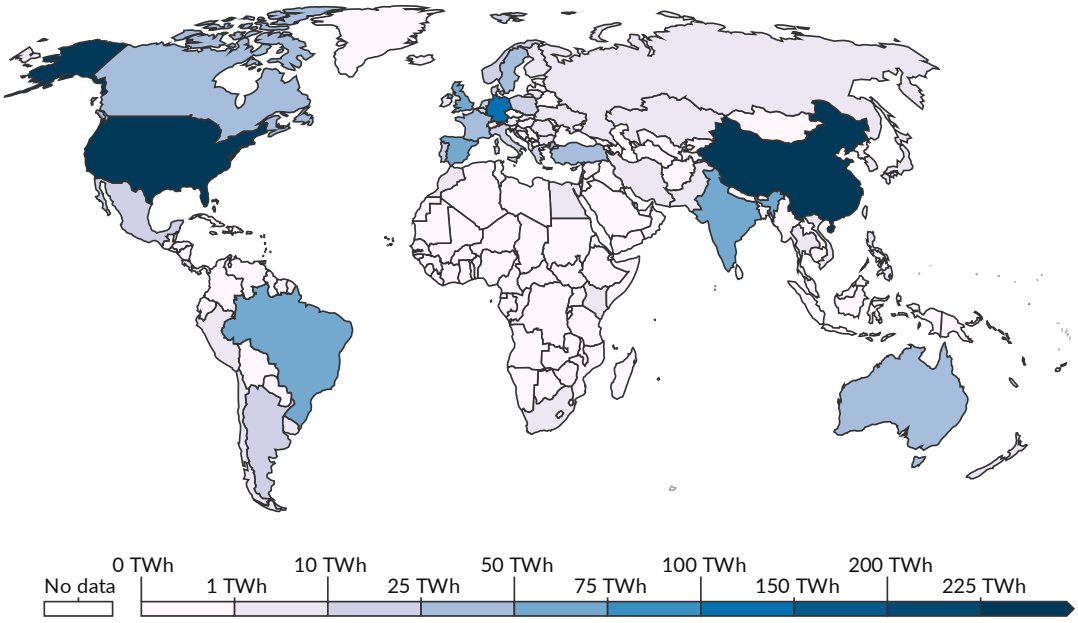

Figure 1.1.10: Wind power generation, 2021, Annual electricity generation from wind is measured in TWh per year Source: Our World in Data [14].

The wind turbines can be divided in two main categories based on the installation location, onshore and offshore wind turbines (Fig 1.1.11). Onshore wind farms are installed on land, offshore are installed over open water [13]. Therefore the offshore wind farms have an acoustic and visual impact very trivial respect with the onshore ones.

Using wind energy to produce hydrogen is the cleanest and simplest mechanism in terms of producing emissions and cost/energy compared [11] to other renewable sources. However, this solution has some difficulties to overcome, which are mature wind turbine structure, having electrolyser that accepts wind fluctuations, and a suitable hydrogen storage system.

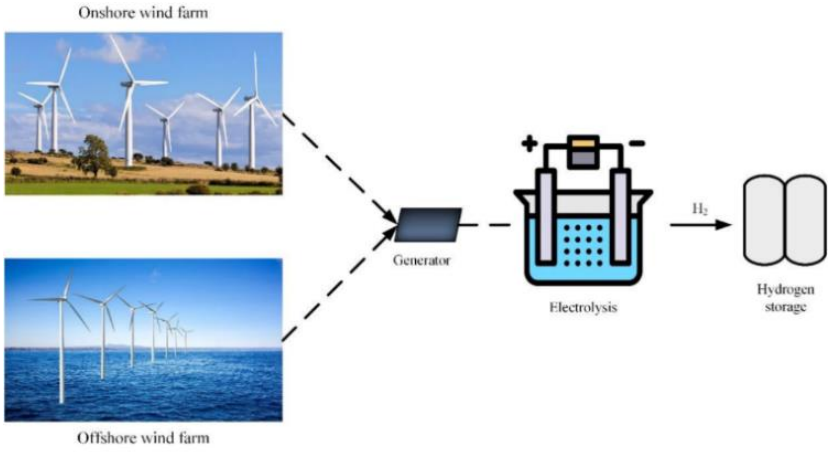

Figure 1.1.11: Onshore and offshore wind energy-driven hydrogen production. [12]

A study reports that the site with the highest wind potential showed hydrogen production 7-226 tons of hydrogen depending on the capacity of the turbine, generating a hydrogen cost equal to about 5 $/kg [11].

A different study regarding an integrated system concluded that the wind/hydrogen system has a better economic performance compared to a regular wind farm. The combination of fuel cells with wind turbines have a vital role in normalizing the wind's fluctuations.

1.1.5. Hydrogen production from biomass

Biomass is a resource available from agricultural residues and agrifoods industrial wastes and municipals organic wastes. It can be used for the generation of biogas, bio-diesel, hydrogen, or even electricity through microbial fuel cells.

Hydrogen is produced from biomass mainly by thermochemical processes and biochemical processes. Thermo-chemical processes require less time compared to the biochemical process. However, thermochemical processes require higher energy input. Also, thermochemical processes have higher efficiency and less cost compared to biochemical.

Thermochemical hydrogen production utilizes typically pyrolysis and gasification of biomass (Fig 1.1.12).

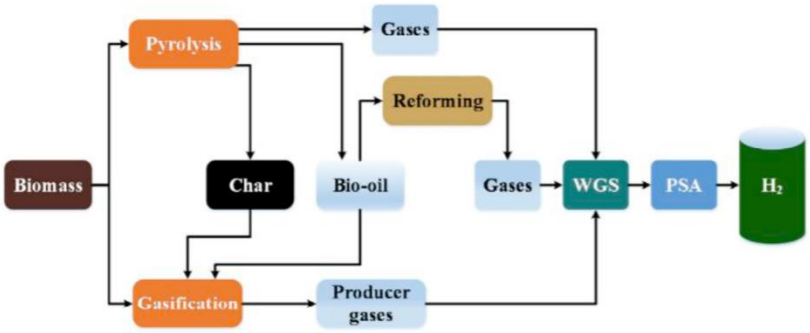

Figure 1.1.12: Hydrogen production schematic using biomass thermochemical conversion: gasification and pyrolysis. [10]

Pyrolysis [10] is a process that can be defined as a high-temperature degradation of organic material, this process produces a mixture of gases or bio-oil, which can be used for hydrogen production. From this method the hydrogen produced is ridiculously small and for this reason the process is not already commercialized.

The biomass gasification is considered one of the most efficient methods for hydrogen production from biomass, and considerably cleaner compared with combustion.

Biomass gasification [13] consists of burning biomass under a limited air supply to create carbon dioxide, hydrogen, methane, carbon monoxide, nitrogen, steam accompanied by other chemicals such as char, tars, and ash particles.

The challenge facing gasification is low efficiency. The researcher conducted several studies for large-scale production of hydrogen through biomass gasification.

1.1.6. Biological hydrogen production processes

The biochemical process is based on micro-organisms that convert organic materials into a mixture of various compounds, including hydrogen. There are different method to produce hydrogen such as dark fermentation and bio-photolysis [18].

1.1.6.1. Dark fermentation

Dark-fermentation [12, 18] is one the most investigated techniques for H_2 production through biological approaches. In this process, hydrogen is produced from a wide range of waste materials (food waste or agricultural waste) or

wastewater using anaerobic organisms Production of hydrogen through dark-fermentation is carried out via the acetate-mediated pathway. The overall reaction stated as follows:

$$C_6H_{12}O_6 + 2H_2O \rightarrow 4H_2 + 2CO_2 + 2CH_3COOH \qquad \Delta G^0 = -206\ kJ$$

The maximum 4 mol of hydrogen generated per 1 mol of glucose are not produced since a part of glucose is routed for microorganisms growth and maintenance.

The yield of the process depends on several factors: pH, temperature, pressure, the type of organism, the presence of metals and composition of the substrate.

Yang et al. added three forestry wastes to sewage sludge in order to enhance hydrogen yield, which is increased by three times. The enhancement of hydrogen yield could be attributed to the increase in C/N ratio of substrate and the presence of high amount of carbohydrate produced during the cofermentation [12].

Some pre-treatment processes are always required to improve the quality of the substrate and also undesired components such as ammonium.

Hydrogen-producing bacteria can be classified as spore-forming obligate anaerobic bacteria, non-sporulating anaerobes and, facultative bacteria. In Fig 1.1.13 the dominant species for each H2 producing population are reported.

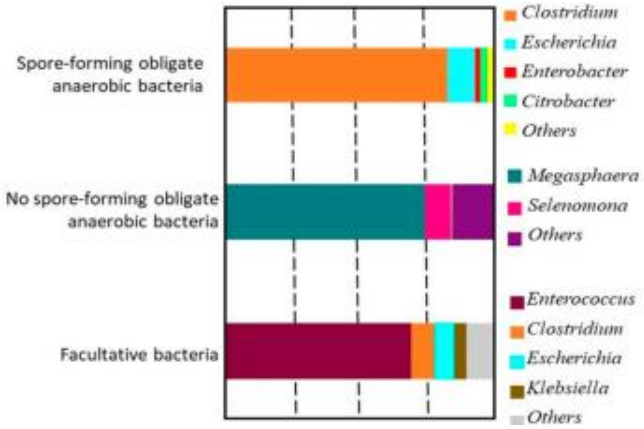

Figure 1.1.13: Three examples of the taxonomic composition of H2-producing communities dominated [12]

1.1.6.2. Bio-Photolysis

The process defined as bio-photolysis [12] is a photonic-driven hydrogen production, in which water splitting is purposed by using cyanobacteria and blue-green algae.

The performance of cyanobacteria is based on catalytic activities of nitrogenase enzyme that is responsible for the low light conversions efficiency, whose maximum is 6%. Whereas the blue-green algae have a high light conversion efficiency in a range between 10 and 13% [18]. These organisms also are able to absorb different emissions of sunlight, near infrared and the visible spectrum, respectively.

The bio-photolysis can be categorized in direct and indirect bio-photolysis.

The direct route [18] consists of a photosynthetic reaction through microalgae:

$$2H_2O + Light\ energy \rightarrow O_2 + 2H_2$$

The indirect bio-photolysis is a two-step process, the first one is the photosynthesis while the second one produces hydrogen and carbon dioxide:

$$12H_2O + 6CO_2 + Solar\ energy \rightarrow 6O_2 + C_6H_{12}O_6$$

$$C_6H_{12}O_6 + 12H_2O + Solar\ energy \rightarrow 6CO_2 + 12H_2$$

The hydrogen production is due to hydrogenase and nitrogenase enzymes. The process can occur directly or indirectly as depicted in Figure 1.1.14.

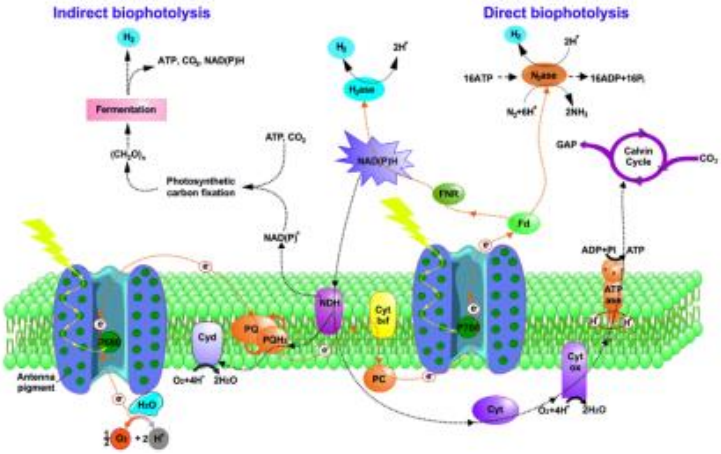

Figure 1.1.14: Direct and indirect bio photolysis processes of photosynthetic microorganisms [12]

1.1.7. Purple hydrogen production method

Today the nuclear energy represents less than 10% of the whole worldwide energy supply. The uranium nuclear fuel resources are more significant than fossil fuels. Since nuclear plants do not generate directly GHG emissions, the only emissions are related with the construction and the maintenance. In Figure 1.1.15 the global production of nuclear energy is reported in TWh per year.

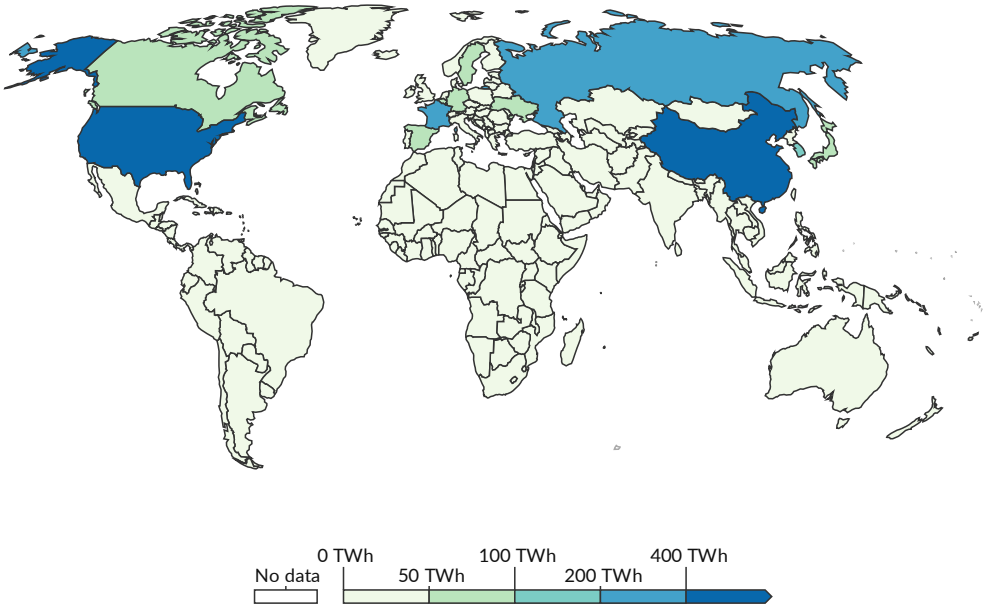

Figure 1.1.15: Nuclear power generation, 2021, Source: Our World in Data [14]

Nuclear energy based hydrogen production is defined as purple hydrogen [13].

Nuclear energy is derived principally from uranium atoms fission. This type of energy source produces heat to generate steam, which can be employed to produce electricity.

In a nuclear power plant, the fission reaction is employed to the reactor which is a heat source of thermal energy. Nuclear energy is generated using atoms splitting in the nuclear reactor which converts water into steam, employed to the turbine and electricity is generated.

In 29 states, 20% of national electricity is produced by ninety-five nuclear plants using uranium [19]. The nuclear reactor is used to perform a fission reaction and generate thermal energy which can be used for multiple purposes. The most common method of utilizing this thermal energy is to produce power using a turbine which can later be employed to the fuel cells for hydrogen production. Some

other methods are to employ this thermal energy to the different processes such as thermochemical water splitting cycles, steam reforming methods, or water electrolysis for hydrogen production.

In the near future methods for obtaining hydrogen using carbon compounds as the raw material will probably be the main methods. However, the raw materials and environmental legislative limitations are stimulating the development and research of methods to produce hydrogen from water. The most promising of these processes for utilization of nuclear power are electrolysis and thermochemical and thermoelectrochemical cycles.

Nuclear power plants produce heat that can be used directly or enrouted to generate to electricity for hydrogen production. In the purple methods it is possible to distinguish between four different classes of options [19, 20], which are reported in Figure 1.1.16:

- Hydrogen production via electrolysis using LWR (Light Water Reactor);
- Hydrogen production via electrolysis using HTGR (high temperature gas-cooled reactor);
- Hydrogen production via high-temperature electrolysis using HTGR (high temperature gas-cooled reactor) (electricity+heat+H_2O→[cyclic chemical reactions]+H_2+O_2);
- Hydrogen production via thermochemical water cracking (heat+H2O→[cyclic chemical reactions]+H_2+O_2).

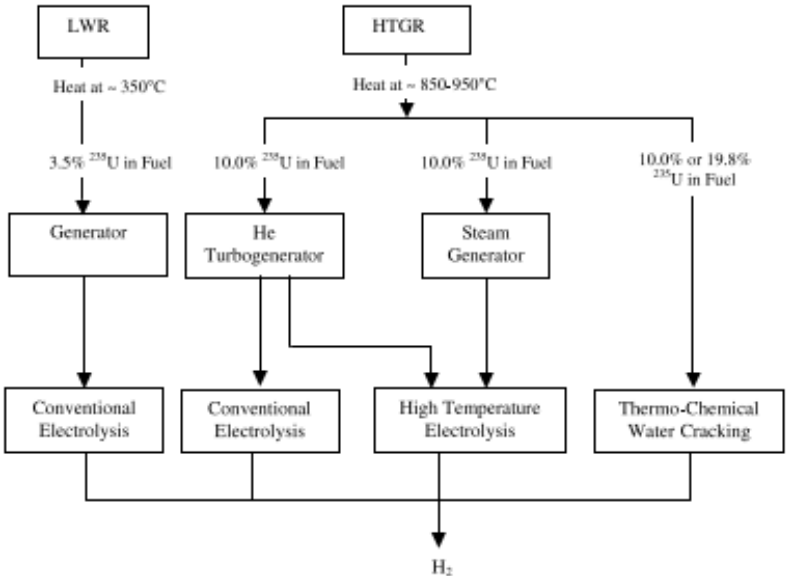

Figure 1.1.16: Four principal production strategy of hydrogen using nuclear reactors [19]

Electrolysis is a short-term option while the use of heat to convert water to hydrogen and oxygen is a long-term strategy because heat is less expensive than electricity, the cost avoided are related to heat conversion to electricity with associated losses. These advanced processes belong to the long-term options for potential reduction of production costs.

1.2. State of the art in hydrogen production by using plasma

The production of hydrogen represents a promising technological solution for the development of an energy vector that is a sustainable and relatively energy efficient. Several H2 production processes have reached maturity for commercial exploitation such as steam methane reforming (SMR), partial oxidation, catalytic methane decomposition (CMD), and coal gasification, while other H2 sources are being developed such as electrochemical processes, thermochemical water-splitting, biomass gasification, and bio-processes, as discussed in the previous section. Currently, the first source for hydrogen production are fossil fuels, especially natural gas.

Since the EU goal is to minimize the greenhouse gases emissions, the CO2 must be managed through sequestration causing an increase in the final cost of the produced hydrogen.

In order to limit environmental impacts, new environmentally friendly alternatives are investigated. A promising one is thermal methane dissociation into hydrogen and carbon black, which are two valuable products.

The most commonly used plasma types are dielectric barrier discharges (DBDs), microwave (MW), and gliding arc (GA) plasmas.

The plasmas can be divided into two macrocategories: non-thermal and thermal plasma.

The first plasma category includes the systems which exist very far from the thermodynamic equilibrium. This condition leads to describe them by multiple diffrent temperatures depending on different plasma particles. The heavy particles temperature is much smaller than that of electrons. In this system the ionization and

chemical properties are dependent on the electronic rather than the thermal temperature. For that reason these systems are called non-thermal plasma.

The second plasma category, the so-called thermal plasma, is characterized by Local Thermodynamic Equilibrium (LTE) in plasma where the temperatures of electrons and heavy particles approach each other. An additional requirement for LTE is the chemical equilibrium so that, the system can be described by a single temperature at each spatial point. The ionization and chemical properties are determined directly by temperature and indirectly by the electric field.

The performance in terms of conversion and selectivity toward different hydrocarbons is different depending on plasma types, in tables 1.1 and 1.2 are reported the non-thermal plasma SER (specific energy requirement, expressed as kWh/Nm^3_{H2}) and the thermal plasma SER, respectively. The SER parameter defines how much energy is required to produce a Normal cubic meter of hydrogen. As a consequence, SER is the right parameter to provide a proper comparison of different existing technologies. For each type of plasma reactor are reported also the methane conversion and the process methane flow rate.

In table 1.1 different non-thermal plasma reactors are tabulated and compared on the base of SER parameter.

The first type considered is the mobile and elongating arc plasma reactor [21], whose electrodes consist of a set of screw type helix and a rod-like electrode. The peculiar setting (Fig. 1.2.1) of this reactor allows to investigate how the arc elongation and the angular velocities affect the performances of such reactor.

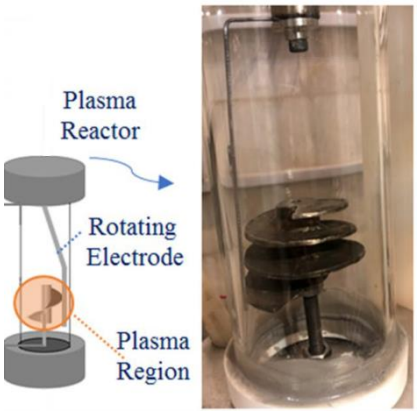

Figure 1.2.1: Mobile and Elongating Arc Plasma Reactor. [21]

The second plasma reactor analyzed is the microsecond pulsed spark reactor [22].

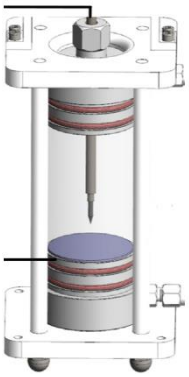

Figure 1.2.2: Settings of microsecond pulsed spark reactor. [22]

In this particular reactor the high voltages electrode used is a needle-head rod, while the ground electrode is a steel plate (Fig 1.2.2). The frequency of microsecond pulsed spark discharge is imposed by a pulse power source. This type of reactor are more efficient by 33% in energetic term with respect to microsceond pulsed with corona electrode.

A different version of pulsed reactor considered is the nanosecond pulsed dielectric barrier discharge (DBD) [23]. The discharge is controlled in the same way of the previous reactor, but here the high voltage electrode (inner one) is separated from the reaction chamber by a dielectric material (i.e. plexiglass) while a copper foil (outer electrode) is wrapped around the quartz tube. This setup (Fig. 1.2.3.) leads to a more uniform discharge zone.

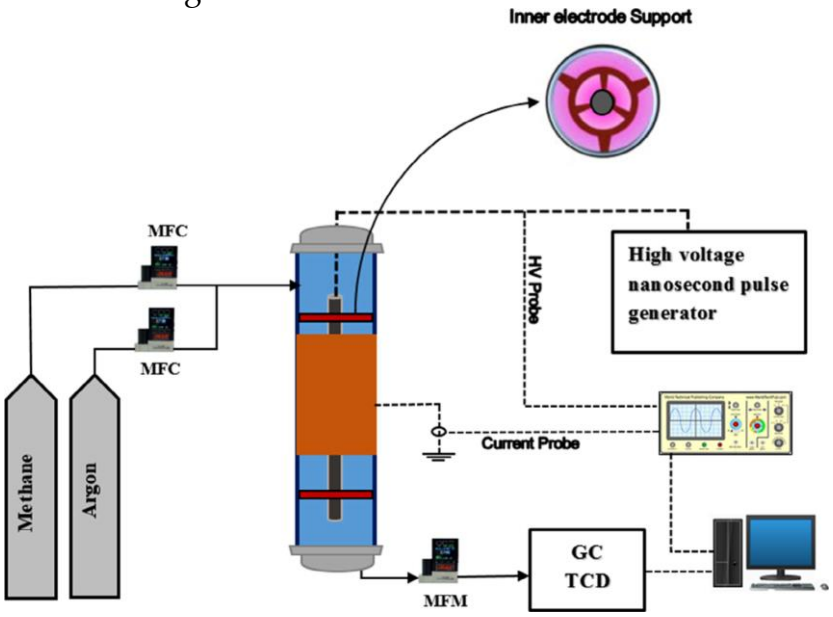

Figure 1.2.3: Schematic diagram of nanosecond pulsed DBD setup. [23]

The rotating gliding arc [24] is another non-thermal plasma reactor object of our investigation. In this setup (Fig 1.2.4) the inner electrode through the rotation permits a homogeneous distribution of the species improving the reactor performances.

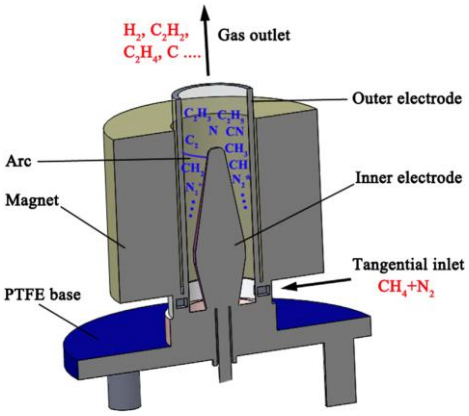

Figure 1.2.4: Configuration of the RGA discharge reactor. [24]

The microwave plasma [25] can be induced in different manners. The case reported in Table 1.1 the waveguide-supplied metal-cylinder-based microwave plasma reactor. An overall diagram of the experimental configuration is depicted in Fig. 1.2.5.

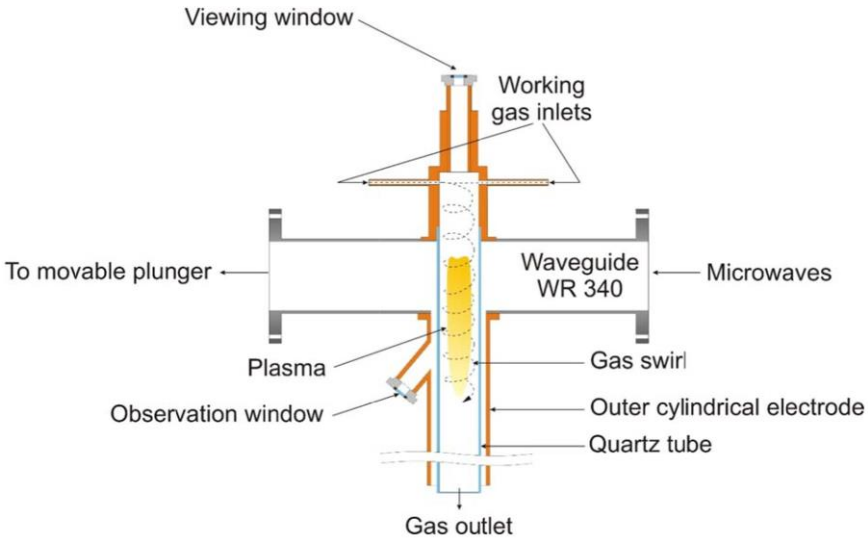

Figure 1.2.5: Configuration of a waveguide-supplied metal-cylinder-based microwave plasma reactor. [25]

In Table 1.2 the different thermal plasma SER of several reactor are reported.

The first reactor considered is the PlasGas [28] reactor depicted in Fig 2.1.6. Plasma torch is attached at the top of the reactor. The reactor is designed to ensure a complete mixing of plasma with treated substances.

The second reactor is the Radio Frequency Thermal Plasma reactor [29]. Usually this type of discharge is used to produce carbon black. Through this type of torch reactor it is possible to approach a total methane conversion. Its configuration is reported in Fig. 1.2.7

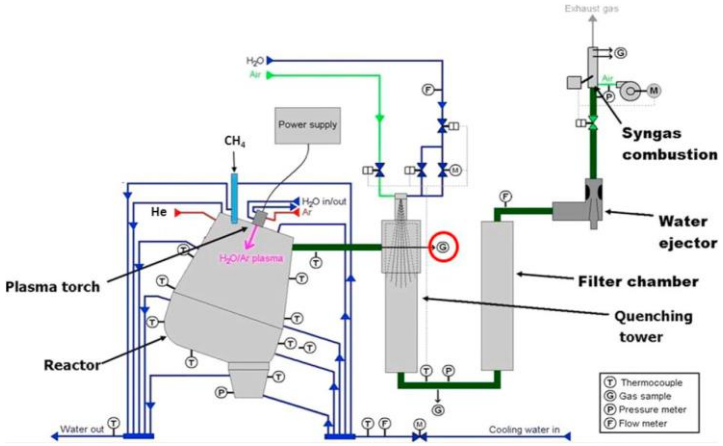

Figure 1.2.6: Configuration of PlasGas reactor. [28]

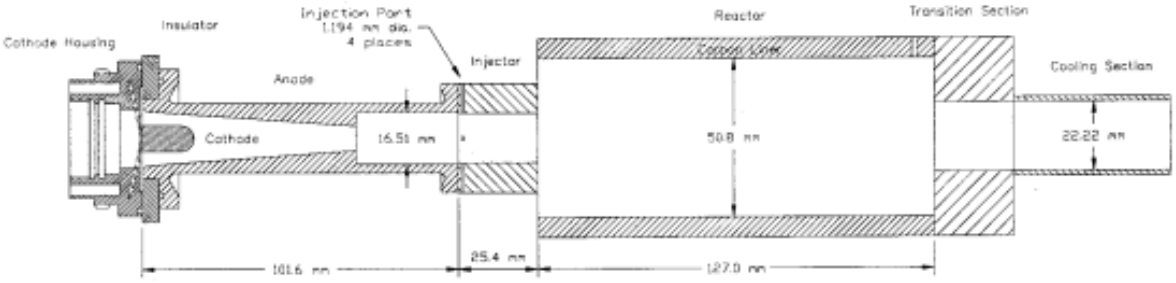

Figure 1.2.7: Schematic of torch, injector, and reactor; flow is left to right. [29]

In the Table 1.3 different strategies for Catalytic Methane Decomposition are listed. For each type of process the main available parameters are reported. The two most important ones are the Specific Energy Requirement and the methane conversion.

Table 1.1: Non-Thermal Plasma Specific Energy Requirement (SER)

Non-thermal plasma			
Technology	**Methane flow rate**	**Methane conversion**	**Experimental SER (kWh/m3.H2)**
Mobile and Elongating Arc Plasma Reactor with single turn [21]	150 mL/min	0.24-0.44	2.60-4.495
Mobile and Elongating Arc Plasma Reactor with double turn [21]	150 mL/min	0.47-0.43	2.43-2.67
Mobile and Elongating Arc Plasma Reactor with triple turn [21]	150 mL/min	0.44-0.41	2.61
Microsecond pulsed spark [22]	50 mL/min	0.912	10.58
Nanosecond pulsed DBD [23]	10 mL/min	0.25	37.15
Pulsed plasma [23]	200 mL/min	0.45	6.57
Rotating gliding arc [24]	24000 mL/min	0.17	3.98
Microwave [25]	175000 mL/min	0.132	1.057
Stationary discharge plasma [25]	150 mL/min	0.25	4.915
One-dimensional mobile plasma [25]	100 mL/min	0.45	4.086
Gliding arc plasma, NT CH4/N2 [26]		0.3-0.5	6.94-8.33
Gliding arc plasma, NT CH4/Ar [26]		0.48-0.52	6.11-12.8
Gliding arc plasma, NT CH4/CO2 [26]		0.19-0.62	11.1-25
Non-thermal plasma dielectric barrier discharge reactor [27]	20 mL/min	0.07-0.35	

Table 1.2: Thermal plasma Specific Energy Requirement (SER)

Thermal plasma			
Technology	**Methane flow rate**	**Methane conversion**	**Experimental SER (kWh/m3.H2)**
Plasgas reactor [28]	200 slm	0.805	2.085
	300 slm	0.75	1.853
	500 slm	0.61	1.140
RF plasma torch [29]	120.8 slm	0.991	1.420
	90 slm	0.994	1.187
Plasma-catalyst hybrid system [21]	10 mL/min	0.874	499.44
DBD, dielectric barrier discharge [21]	25 mL/min	0.35	272.4

Table 1.3: Catalytic decomposition of methane (CDM) Specific Energy Requirement (SER) (if available) and other important data

Catalytic methane decomposition					
Technology	**Methane flow rate**	**Methane conversion**			
Fixed-bed quartz reactor heated by an electric furnace [30]			**g of C/ g Fe**	**Cost in $ per hydrogen mole**	
Iron concentrate powder (Fe-IP)	50 mL/min	0.55-0.7	3.8	0.0007	
Fine ash (Fe-FA)	50 mL/min	0.6	2.4	0.0011	
Coarse ash (Fe-CA)	50 mL/min	0.4-0.2	1.6	0.0017	
Steel slag (Fe-SS)	50 mL/min	0.15-0.45	3.3	0.0008	
Volcanic mud powder (Fe-VP)	50 mL/min	0.03	0	-	
Pure iron (Fe-PI)	50 mL/min	0.5-0.6	4	0.000665	
800 °C under atmospheric pressure fixed-bed flow reactor heated; Mo/MgO	60 mL/min		**C yield**	**H2 yield**	

getting carbon nanotubes (CNTs) or carbon nanofibers (CNFs) [31]					
20% Mo			0.8	0.22-0.48	
30% Mo			1.66	0.48-0.66	
40% Mo			1.8	0.39-0.68	
50% Mo			1.4	0.75-0.59	
Natural Fe-based catalysts fixed bed reactor [32]	50 mL/min 10%				
Tierga 900 °C	2 L/(g_{cat}*h)	0.67-0.53			
Tierga 850 °C	2 L/(g_{cat}*h)	0.41-0.56			
Tierga 800 °C	2 L/(g_{cat}*h)	0.3-0.32			
Ilminite 800 °C	2 L/(g_{cat}*h)	0.08-0.1			
Rice husk derived silica [33]			**mmol H2 per g silica**	**g C per g silica**	**SER**
SiO2/100	200 cm^3/min		14	0.09	23.57
SiO2/250	200 cm^3/min		1	0.01	217.64
aw-SiO2/100	200 cm^3/min		140	0.84	5.49

aw-SiO2/250	200 cm^3/min		72	0.48	4.33
Carbon encapsulated Iron nanoparticles [34]		**Methane conversion**		**g Carbon/g catalyst**	
Temperature		**700 °C**	**800 °C**	**700 °C**	**800 °C**
20 CEINP	100 mL/min	0.63-0.15	0.9-0.2	0.18	0.28
30 CEINP	100 mL/min	0.7-0.2	0.96-038	0.21	0.39
40 CEINP	100 mL/min	0.5-0.2	0.85-0.38	0.18	0.36
CeO2 loaded hydrotalcite (MgNiAl) catalyst [35]		**Methane conversion**		**H2 selectivity**	
MNA		0,51		0.35	
CeO2		0,49		0.36	
5% CeO2-MNA		0,68		0.38	
10% CeO2-MNA		0,92		0.45	
15% CeO2-MNA		0,87		0.4	

1.3. Conclusions and aim of the thesis

The conventional process of methane steam reforming leads to significant GHGs emissions. It was estimated that the global warming potential (GWP) of hydrogen production via the SMR process is 13.7 kg CO_2eq per kg of H_2 produced (CO_2 accounts for 77.6% of the system's GWP) .

The aim of the thesis is to investigate the plasma thermal conversion of methane to hydrogen.

The intent is to find an effective strategy to minimize the energy consumption maximizing at the same time the yield of carbon black and hydrogen. The predictions of the developed model will be tested over experimental data measured in a plasma torch whose performances have been described in the literature.

In addition, in the thesis different conditions will be explored to investigate their impact on methane conversion to carbon and acetylene, as well as to better understand the mechanism of carbon formation in the investigated plasma reactor configuration.

2 Methods

In this section the theoretical models used to investigate methane conversion through plasmas are reported. In order to get an adequate description of this complicated process a schematization consisting of three steps was adopted: methane conversion in the plasma discharge, the mixing between the gas exiting the discharge and the by-pass, and the final reactive cooling down stage. For the first step the purpose of the model is to compute an estimate of temperature and composition in the arc discharge area. In the mixing stage it is estimated the composition assuming that mixing leads to rapid thermal and thermodynamic equilibrium. This step is the result of mixing the flow rate from the plasma arc discharge and the gas bypassing the arc. The last step investigated is the system reactivity determined by cooling down the high temperature reactive mixture. In this modeling step the attention is focused on soot formation.

Plasma discharge model

2.1.1. The Steenbeck-Raizer Model of the thermal arc discharge

The aim of the Steenbeck-Raizer model is that of predicting, on the basis of operating parameters of the arc discharge, its main features, and in particular the radius of the arc r_0, the average temperature reached in the arc (T_m) and the mean electric field (E). The model was developed first by Max Steenbeck [36] in 1932. The model of the German physicist was reviewed by Yuri Raizer in 1974 [37, 38].

The model requires the solution of a set of three equations, which are developed as described in the following.

One of the main assumptions of the model is that the arc current is confined in a channel of radius r_0. In the formulation of the model (and in standard operating conditions for plasma arcs) the current is the experimentally controlled parameter, and can be expressed as a function of the electric field (E) as

$$I = E \int_0^{r_0} \sigma[T(r)]\, 2\pi r\, dr \qquad (3.1)$$

Where $\sigma[T(r)]$ is the electric conductivity of the plasma and R is the radius of the chamber where the arc is placed. Assuming an average thermal conductivity, current and electric field can thus be related as:

$$I = E\ \sigma_m \pi r_0^2 \tag{3.2}$$

Introducing the power deposited in the discharge per unit of length $W_L = IE$, we can then obtain the first equation we are looking for, which relates power to current, radius and average conductivity:

$$W_L = \frac{I^2}{\pi r_0^2 \sigma_m} \tag{3.3}$$

The temperature distribution in a long cylindrical steady-state thermal plasma column stabilized by walls in a tube of radius R is described by the Elenbaas-Heller equation, assuming heat transfer across the positive column provided by heat conduction with the coefficient λ(T). According to Maxwell equations, in the absence of a magnetic field $\nabla \times \mathrm{E} = 0$, so that the electric field in a long homogeneous arc column is radially constant. The energy balance equation can thus be expressed in the Elenbaas-Heller form as:

$$\frac{1}{r}\frac{d}{dr}\left[\mathrm{r}\lambda(\mathrm{T})\ \frac{\mathrm{dT}}{dr}\right] + \sigma(\mathrm{T})\mathrm{E}^2 = 0 \tag{3.4}$$

Introducing the heat flux potential Θ(T) defined as:

$$\Theta = \int_0^T \lambda(T)dT$$

We obtain:

$$\lambda(T)\frac{dT}{dr} = \frac{d}{dr}\Theta$$

Which substituted in equation 3.4 gives:

$$\frac{1}{r}\frac{d}{dr}\left[\mathrm{r}\ \frac{\mathrm{d}\Theta}{dr}\right] + \sigma(\Theta)\mathrm{E}^2 = 0 \tag{3.5}$$

Outside of the channel r > r0; electric conductivity, current, and Joule heating can be neglected. The Elenbaas-Heller equation can thus be integrated with the boundary conditions T = T_m at r = r0 and T = 0 by the walls at r = R assuming a constant σ_m value. The integration gives the relation between the heat flux potential

$\Theta_m(T_m)$ related to the plasma temperature and the discharge power per unit length, $W_L = IE$, and is the second of the equations of the Raizer model:

$$\theta_m(T_m) = \frac{W_L}{2\pi}\ln\frac{R}{r_0}, \tag{3.6}$$

Steenbeck suggested the principle of minimum power as the third equation to complete the system. The minimum power principle has been proved for arcs by Rozovsky in 1972. According to the principle of minimum power, temperature T_m and arc channel radius r_0 should minimize the specific discharge power W_L and electric field E.

But Raizer finally proved that the channel model does not require the minimum power principle to justify the third equation. It can be derived by analysis of the conduction heat flux J_0 from the arc channel, $W_L = 2\pi r_0 J_0$, expressed as a function of the temperature difference $\Delta T = T_m - T_0$ across the arc:

$$J_0 = \lambda_m(T_m)\frac{\Delta T}{r_0} = \lambda_m(T_m)\frac{T_m - T_0}{r_0}$$

Integrating the Elenbaas-Heller equation inside of the arc $0 < r < r_0$ leads to the relation:

$$4\pi\Delta\Theta = W_L \approx 4\pi\lambda_m\Delta T, \tag{3.7}$$

$$\Delta\Theta = \Theta_m - \Theta_0$$

The key point of the Raizer modification of the channel model is the assumption of an arc channel as a region where electric conductivity does not decrease by more than e=2.718… times with respect to the maximum value at the axis. The mean electric conductivity $\sigma_m$is related to the ionization potential by the Saha equation [39]:

$$\sigma_m = C\exp\left(-\frac{I_i}{2T_m}\right) \tag{3.8}$$

Since the e-times decrease of conductivity, the temperature decrease results to be small since the Saha equation and expressed as:

$$\Delta T = T_m - T_0 = \left(\frac{2T_m}{I_i}\right) * T_m = \frac{2T_m^2}{I_i}$$

Substituting this expression in equation (3.7), it is then possible to derive the third equation of the Raizer model:

$$W_L = \frac{8\pi\lambda_m(T_m)T_m^2}{I_i} \tag{3.9}$$

Where I_i is the average ionization potential expressed in thermal units (K). Equations (3.3), (3.6) and (3.9) are a system of three equations in the three unknowns, which can be solved after noting that $\theta_m(T_m) = \lambda_m T_m$, and that Saha equation.

The unknowns are therefore: T_m, r_0 (radius of plasma column)raiser, E (electric field).

- W_L is discharge power per unit length
- R is the discharge tube radius
- θ_m is the heat flux potential
- λ_m heat conductivity
- I_i ionization potential

Average values of C, I_i and λ_m are determined for our working range of temperature. The following substitutions allow to obtain an analytic solution of the considered set of equations.

2.1.1.1. Solution of the system describing the thermal plasma

The first step is to compare the equations (3.6) and (3.9):

$$\frac{8\pi\lambda_m(T_m)T_m^2}{I_i} = \frac{2\pi\,\theta_m(T_m)}{\ln\frac{R}{r_0}} \tag{3.10}$$

$$\frac{8\pi\lambda_m(T_m)T_m^2}{I_i} = \frac{2\pi\,\lambda_m T_m}{\ln\frac{R}{r_0}}$$

$$\frac{4T_m}{I_i} = \frac{1}{\ln\frac{R}{r_0}} \tag{3.11}$$

$$\frac{I_i}{2\,T_m} = \ln\frac{R^2}{r_0^2} \tag{3.12}$$

$$\sigma_m = C\exp\left(-\frac{I_i}{2T_m}\right)$$

$$\sigma_m = C\exp\left(-\ln\frac{R^2}{r_0^2}\right)$$

$$r_0^2 = \frac{R^2 \sigma_m}{C} \tag{3.13}$$

From that comparison a relation which links r_0 and R (3.13) is obtained.

The subsequent step is confronting the equations (3.3) and (3.6):

$$\frac{8\pi\lambda_m(T_m)T_m^2}{I_i} = \frac{I^2}{\pi r_0^2 \sigma_m} \tag{3.14}$$

$$\sigma_m = \frac{I^2\, I_i}{\pi r_0^2\, 8\pi\lambda_m T_m^2}$$

$$\sigma_m = \frac{I^2\, I_i\, C}{\pi^2 \sigma_m R^2\, 8\lambda_m T_m^2}$$

$$\sigma_m = I\sqrt{\frac{I_i\, C}{\pi^2 \sigma_m R^2\, 8\lambda_m T_m^2}} \tag{3.15}$$

From the equalizing a first expression for the electric conductivity.

Then Saha equation (3.8) and the (3.15) can be equated:

$$C\exp\left(-\frac{I_i}{2T_m}\right) = I\sqrt{\frac{I_i\, C}{\pi^2 \sigma_m R^2\, 8\lambda_m T_m^2}} \tag{3.16}$$

$$\exp\left(-\frac{I_i}{2T_m}\right) = I\sqrt{\frac{I_i}{C\,\pi^2 \sigma_m R^2\, 8\lambda_m T_m^2}}$$

$$\frac{I_i}{2T_m} = \ln\sqrt{\frac{C\,\pi^2 \sigma_m R^2\, 8\lambda_m T_m^2}{I_i\, I^2}}$$

It is now possible to deduce the first unknown T_m:

$$T_m = \frac{I_i}{\ln\left(C\frac{8\pi^2\lambda_m T_m^2}{I_i}\right) - 2\ln\left(\frac{I}{R}\right)} \tag{3.17}$$

From the relation $\omega = IE$ the electric field can be expressed as:

$$E = \frac{\omega}{I} = \frac{8\pi\lambda_m(T_m)}{I}\frac{I_i}{\left(\ln\left(C\frac{8\pi^2\lambda_m T_m^2}{I_i}\right) - 2\ln\left(\frac{I}{R}\right)\right)^2} \tag{3.18}$$

The following expression for the radius of plasma arc r_0 is the last relation derived from the considered set of equations:

$$r_0 = R\sqrt{\frac{\sigma_m}{C}} = R\sqrt{\frac{I}{R}}\sqrt[4]{\frac{I_i}{8\,\pi^2\lambda_m T_m^2\,C}} \tag{3.19}$$

2.1.2. Alternative models of plasma arcs

In addition to the Steenbeck-Raizer system it is possible to develop a model for the plasma discharge starting from the elementary formula for ideal plasma electrical conductivity, which can be defined as:

$$\sigma = \frac{e^2 n_e}{m_e \nu_{eff}} \tag{3.20}$$

where e is the elementary charge, m_e and n_e are the electron mass and density, while ν_{eff} is the effective electron-ion collision frequency.

The second equation that must be considered is the Saha equation (3.8) in a modified version:

$$\frac{n_e n_i}{n_a} = \frac{2Q_i(T)}{Q_a(T)}\left(\frac{m_e k_B T}{2\pi\hbar^2}\right)^{\frac{3}{2}} \exp\left(-\frac{I_i}{2T}\right) \tag{3.21}$$

Where Q_i and Q_a are respectively the partition function of the ions and neutral species, and n_i and n_a the ions and neutral species density.

From the relation (3.12) is possible to get an expression defining the electron density:

$$n_e = \frac{2Q_i(T)n_a}{Q_a(T)n_i}\left(\frac{m_e k_B T}{2\pi\hbar^2}\right)^{\frac{3}{2}} \exp\left(-\frac{I_i}{2T}\right) \tag{3.22}$$

Since the high temperature and the quasi neutrality condition at which typically the thermal plasma works it is possible to consider the ratio between the partition function and density close to one. So that the relation (3.22) becomes:

$$n_e = 2\left(\frac{m_e k_B T}{2\pi\hbar^2}\right)^{\frac{3}{2}} \exp\left(-\frac{I_i}{2T}\right) \tag{3.23}$$

While the effective electron collision frequency can be defined as

$$\nu_{eff} = \frac{4\sqrt{2\pi}n_e e^4 \Lambda}{3\sqrt{m_e}T_e^{3/2}} \tag{3.24}$$

Where T_e is the electronic temperature which follows the relation:$T_e = \frac{T}{k_B}$ and Λ is the Coulomb logarithm is function of the electron collision frequency and is expressed as follows:

$$\Lambda = \frac{1}{2}\ln\left(1 + \frac{T_e \varepsilon_0^3 m_e^2 v^4}{4\pi e^6 n_e}\right) \tag{3.25}$$

With the addition of the equation (3.23) in the definition of electric conductivity (3.21), a new expression is obtained:

$$\sigma = \frac{2e^2}{m_e \nu_{eff}}\left(\frac{m_e k_B T}{2\pi\hbar^2}\right)^{\frac{3}{2}} \exp\left(-\frac{I_i}{2T}\right) \tag{3.26}$$

This relation is remarkably similar to the Saha equation (3.8) defined in the previous model, but the parameter C is no more constant but a function of the temperature and other parameters:

$$C = \frac{2e^2}{m_e \nu_{eff}}\left(\frac{m_e k_B T}{2\pi\hbar^2}\right)^{\frac{3}{2}} \tag{3.27}$$

2.2. Plasma thermodynamic model

In previous paragraph two different models to describe the plasma arc properties, especially temperature, have been developed.

In the two following paragraphs the respective model is used to determine equilibrium temperatures in two different situations.

2.2.1. Plasma thermodynamic model, only gaseous phase

The first situation analyzed is the thermodynamics equilibrium of the plasma at different temperature till to see which species are present at the temperature calculated with the plasma arc model.

The program used is the Thermodynamic Equilibrium Eqter software (version May 1997) developed by Cavallotti et al.. The executable program requires as input a series of variables. Specifically, the variables to be inserted are the pressure, the temperature, the species that must be considered for the calculation and the relative initial molar fraction.

In the studied case only the gas phase has been explored, so that the carbon formation is not accounted.

Since the equilibrium is the designated goal, it is necessary to have an adequate number of stoichiometric constraints. In the following analysis the species treated are methane, ethane, hydrogen, ethene, ethyne, benzene, monoatomic hydrogen radical, methyl radical, gaseous carbon and ethynyl radical.

Hence the final system will account for ten species, while the elements are hydrogen and carbon, so that the number of required constraints is due to the difference between the number of species and the rank of element-species, A.

The matrix S and E represent respectively the specie and element.

$$S = [CH_4 \;\; C_2H_6 \;\; H_2 \;\; C_2H_4 \;\; C_2H_2 \;\; C_6H_6 \;\; H \;\; CH_3 \;\; C \;\; C_2H]^T$$

$$E = [C \;\; H]$$

$$A = \begin{bmatrix} 1 & 2 & 0 & 2 & 2 & 6 & 0 & 1 & 1 & 2 \\ 4 & 6 & 2 & 4 & 2 & 6 & 1 & 3 & 0 & 1 \end{bmatrix}$$

The rank of considered element-species matrix A is equal to two, so that the necessary number of stoichiometric constraints is equal to eight.

For the corresponding equilibrium, these eight relations are chosen:

1. $2CH4 \rightarrow H2 + C2H6$

2. $2CH4 \rightarrow C2H4 + 2H2$
3. $C2H4 \rightarrow C2H2 + 2H2$
4. $3C2H2 \rightarrow C6H6$
5. $H2 \rightarrow 2H$
6. $C2H4 \rightarrow H2 + 2CH3$
7. $CH4 \rightarrow 2H2 + C$
8. $C2H2 \rightarrow C2H + H$

From this system of equations the obtained output are the final molar fraction of each of the ten species involved in the simulation at the temperature and at the pressure imposed.

The results obtained from a series of simulation are reported in Chapter 3.1.1.

2.2.2. Plasma thermodynamic model with solid formation

The second situation analyzed is the thermodynamic equilibrium of the plasma as a function of temperature to observe which species are present at the imposed temperature, also considering the formation of solid species.

The program used is the Thermodynamic Equilibrium Eqsol software (version May 2022) developed by Cavallotti et al. The executable program requires a series of variables as input.

Specifically, the variables to be inserted are the pressure in torr, the temperature in Celsius degree, the species that must be considered for the calculation and the relative initial composition. The program can be used also to calculate iteratively the equilibrium in a certain temperature range at a given step.

In the studied case the formation of solid carbon is investigated to observe under which condition it occurs in the most effective way.

Since the equilibrium is a given assumption, an essential requirement is to have the adequate number of stoichiometric constraints. In the following analysis the species treated are methane, ethane, hydrogen, ethene, ethyne, benzene, monoatomic hydrogen radical, methyl radical, gaseous carbon, ethynyl radical, argon and solid carbon. Obviously, Argon is not a reacting species, so that the final system will account for eleven species, while the elements are hydrogen and carbon, so that the number of required constraints is due to the difference between the number of species and the rank of element-species, A.

The matrix S and E represent respectively the reactive specie and element.

$$S = [CH_4 \;\; C_2H_6 \;\; H_2 \;\; C_2H_4 \;\; C_2H_2 \;\; C_6H_6 \;\; H \;\; CH_3 \;\; C \;\; C_2H \;\; C_{sol}]^T$$

$$E = [C \;\; H]$$

$$A = \begin{bmatrix} 1 & 2 & 0 & 2 & 2 & 6 & 0 & 1 & 1 & 2 & 1 \\ 4 & 6 & 2 & 4 & 2 & 6 & 1 & 3 & 0 & 1 & 0 \end{bmatrix}$$

The rank of considered element-species matrix A is equal to two, so that the necessary number of stoichiometric constraints is equal to nine.

For the corresponding equilibrium, these nine relations are chosen:

1. $2CH_4 \rightarrow 3H_2 + C_2H_2$
2. $2CH_4 \rightarrow C_2H_4 + 2H_2$
3. $H_2 \rightarrow 2H$
4. $C_2H_4 + H_2 \rightarrow 2CH_3$

5. $CH4 \rightarrow C + 2H2$
6. $C2H2 \rightarrow C2H + H$
7. $2CH4 \rightarrow H2 + C2H6$
8. $3C2H2 \rightarrow C6H6$
9. $CH4 \rightarrow Csol + 2H2$

From this system of equations the obtained output are the final molar fraction of each of the ten species involved in the simulation at the temperature and pressure imposed. But differently of the results obtained through the eqter, there two different molar fractions, one referred to the solid phase, the other referred to the gaseous one. For that reason, the eqsol program returns two additional output parameter: gas and Pro parameter.

The two parameters are defined as follows:

$$gas = \frac{moles\ of\ gaseous\ phase\ n_{gas}}{total\ moles\ present\ n_{tot}}$$

$$Pro = \frac{total\ moles\ present\ n_{tot}}{initial\ moles\ n_0}$$

Hence for depicting the composition under different temperatures, pressures, and initial compositions it is required to define an initial amount of moles, which is necessary to compute the composition at the equilibrium.

The moles of solid carbon are defined as:

$$n_{Csol} = Pro * n_0 * (1 - gas)$$

While the moles of gaseous phase can be calculated as:

$$n_{gas} = gas * Pro * n_0$$

The results derived from the performed simulations are reported in Chapter 3.1.2.

2.3. System reactivity after plasma-bypass mixing

The last stage to be investigated in the plasma reactor is the section that follows the mixing between the plasma discharge and the gas bypass. The OpenSMOKE++ suite [40, 41] was used to study the reactivity of the system formed after the mixing of the gas passing from the arc and the bypass, whose composition was computed assuming equilibrium, as described in the previous section.

The OpenSMOKE++ suite is composed by a set of standard solvers able to perform 0-D and 1-D numerical simulations [40, 41]. The entire framework is written in object-oriented C++.

The solvers structure of this suite [40, 41], depicted in Fig.2.3.1 includes:

- The kinetic pre-processor, a solver useful to pre-process kinetic mechanisms written in the CHEMKIN format, the thermodynamic data, and the transport data. This utility extracts the required data for each species and reaction, generating a file written in XML format. In this file all needed data are available for describing the entire kinetic model.
- A collection of solvers, precisely an independent executable file for each system to simulate. The suite offers the dedicated solver for a Plug Flow Reactor, for a Batch reactor and so on. Each solver is independent from each other, but it requires the pre-processed XML file containing the kinetic, thermodynamic and transport data.
- The last solver is a graphical post-processor useful to perform the usual plots and also sensitivity analysis.

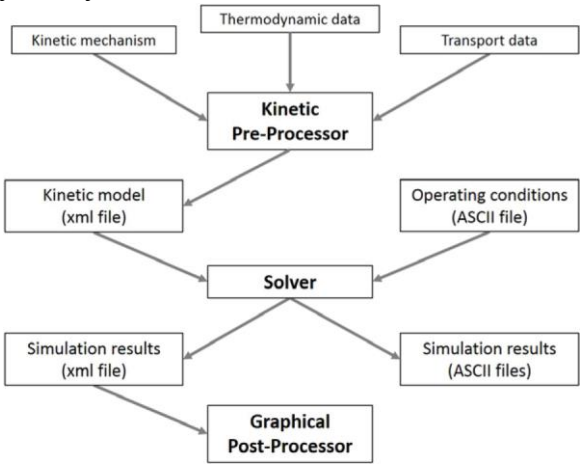

Figure 2.3.1: Structure of OpenSMOKE++ suite. [40, 41]

The simulations performed to study the reactivity that follows the exit from the mixing zone is the plug flow reactor model. This is apt to model the experimental plasma torch system of Fincke et al. [29], who used two reactors with same diameter but different pressures and with different lengths and inlet compositions to convert methane to hydrogen and carbon.

Along the Plug Flow Reactor (PFR) the species and the temperature may vary, but the variations in radial directions are neglected. The equations that rule the system are written as a function of the spatial coordinate ξ and are reported below.

$$\rho v \frac{d\omega_i}{d\xi} = W_i \dot{\Omega}_\iota \quad i = 1, \dots, N_S \tag{2.28}$$

$$\rho v \left(\widehat{C_p} + \frac{v^2}{T} \right) \frac{dT}{d\xi} = \sum_{i=1}^{N_S} \dot{\Omega}_\iota \widetilde{H_\iota} - v^2 W_{mix} \sum_{i=1}^{N_S} \dot{\Omega}_\iota + \frac{UP_c}{A_C} (T_{env} - T) \tag{2.29}$$

$$\frac{d\tau}{d\xi} = \frac{1}{v} \tag{2.30}$$

Equation 2.28 describes the conservation of species, while equation 2.29 is referred to the energy balance, where P_c and A_c are respectively the perimeter and the area of the cross section surface. The last equation, 2.30, is an additional one to return the residence time τ.

To perform adequately the simulations of ideal reactors as PFRs, the user has to define a proper dictionary inserting the instructions. In the observed cases, the dictionaries of our interests are referred to as PFR settings, the soot model, and the temperature profile.

In the Plug Flow Reactor dictionary we have defined the type of reactor: in this case the chosen type is isothermal since a temperature profile is imposed. Then the length and the diameter are inserted in this section of the input. For the investigated system it is considered the molar flow rate, but it would be possible to insert the gas velocity or the mass flow rate instead of mole one.

In the soot dictionary, defined in OpenSMOKE++ suite as PolimiSoot [40, 41], are expressed the settings to be imposed on the soot formation in the reactors of our interest.

The soot particles are defined as default BIN. The BIN particles and their corresponding radicals BINJ are constituted of 25 classes of pseudo species describing heavy Polycyclic Aromatic Hydrocarbons (PAHs), soot aggregates and soot particles.

Each class of BIN/BINJ is described by a specific number of carbon atoms, equivalent spherical diameter, molecular weight, and H/C ratio which subdivides each class in three subclasses defined as A, B and C. The specific number of carbon atom doubles as you move from one class to the next. In tables 2.1, 2, 3 all the properties are reported respectively for Heavy PAHs, soot particles, and soot aggregates.

Table 2.1: Properties of Heavy PAHs

Heavy PAHs						
BINiJ	nC	Mass [amu]	D_P [nm]	H/C ratio		
				A	B	C
BIN1(J)	20	250	0.81	0.8	0.5	0.2
BIN2(J)	40	500	1.02	0.775	0.4	0.2
BIN3(J)	80	1000	1.28	0.75	0.3	0.1
BIN4(J)	160	2000	1.60	0.725	0.2	0.05

Table 2.2: Properties of Soot Particles

Soot Particles						
BINiJ	nC	Mass [amu]	D_P [nm]	H/C ratio		
				A	B	C
BIN5(J)	320	4E+03	2.02	0.7	0.2	0.0.05
BIN6(J)	640	8E+03	2.55	0.675	0.2	0.0.05
BIN7(J)	1.25E+03	1.55E+04	3.18	0.65	0.2	0.0.05
BIN8(J)	2.5E+03	3E+04	4.01	0.625	0.2	0.0.05
BIN9(J)	5E+03	6E+04	5.05	0.6	0.2	0.0.05
BIN10(J)	1E+04	1.2E+05	6.37	0.575	0.2	0.0.05

BIN11(J)	2E+04	2.45E+05	8.02	0.55	0.2	0.0.05
BIN12(J)	4E+04	4.9E+05	10.11	0.525	0.2	0.0.05

Table 2.3: Properties of Soot Aggregates

Soot Aggregates						
BINiJ	nC	Mass [amu]	D_P [nm]	H/C ratio		
				A	B	C
BIN13(J)	8E+04	9.7E+05	13.15	0.5	0.2	0.0.05
BIN14(J)	1.6E+05	1.95E+06	19.32	0.475	0.2	0.0.05
BIN15(J)	3.2E+05	3.9E+06	28.38	0.45	0.2	0.0.05
BIN16(J)	6.4E+05	7.8E+06	41.7	0.425	0.2	0.0.05
BIN17(J)	1.25E+06	1.51E+07	60.46	0.4	0.2	0.0.05
BIN18(J)	2.5E+06	3.02E+07	88.82	0.375	0.2	0.0.05
BIN19(J)	5E+06	6.02E+07	130.49	0.35	0.2	0.0.05
BIN20(J)	1E+07	1.21E+08	191.72	0.325	0.2	0.0.05
BIN21(J)	2E+07	2.41E+08	281.67	0.3	0.2	0.0.05
BIN22(J)	4E+07	4.82E+08	413.98	0.3	0.2	0.0.05
BIN23(J)	8E+07	9.64E+08	608.44	0.3	0.2	0.0.05
BIN24(J)	1.6E+08	1.93E+09	894.25	0.3	0.2	0.0.05
BIN25(J)	3.2E+08	3.86E+09	1314.31	0.3	0.2	0.0.05

All these molecules are of great interest in this work since the aim is to maximize hydrogen production together with reducing as much as possible the acetylene (which is considered an undesired product) production. The soot formation is

preferred to C_2H_2 since the solid carbon materials are easier to be managed then a highly reactive gas.

The last fundamental dictionary that must be inserted to set up properly the reaction system is the temperature profile one. The temperature profile has a fundamental role in controlling the rate production of specie of our interest. In this dictionary the profile is reported as a function of the spatial position and the corresponding temperature.

Since the purpose is to maximize the soot formation, it is fundamental to guarantee the right residence time to the precursor chemical species: benzene is a key precursor for PAHs and soot.

The benzene formation can be obtained from acetylene, but it is necessary to provide the right temperature profile to get the right velocity (and so residence time). All these aspects will be properly deepened in the section 3.3.

3 Results

In this section the results regarding the models described previously are reported. Here, as in the previous section, the results are divided for the three different sections that we considered as representative of the plasma torch: the plasma arc discharge, the mixing subsequent to the discharge, and the final reactive section.

For the first step the purpose is to estimate the temperature, the average electric field, and the radius r_0, which describe the column of the arc discharge. In the second part, the diagrams representing the composition at equilibrium at different conditions, with or without solid formation, are reported. In the section where the impact of the presence of an inert on solid formation is considered as well. The last section is dedicated to the results obtained through the OpenSMOKE++ Suite [40, 41]. In this section the attention is focused on the impact of the imposed cooling temperature profile and the reactor diameter on the system reactivity.

3.1. Results of Raizer-Steenbeck model of a plasma discharge

In paragraph 1.1.1. we got three equations to describe the plasma discharge:

$$T_m = \frac{I_i}{\ln\left(C\frac{8\pi^2\lambda_m T_m^2}{I_i}\right) - 2\ln\left(\frac{I}{R}\right)} \tag{3.17}$$

$$E = \frac{\omega}{I} = \frac{8\pi\lambda_m(T_m)}{I}\frac{I_i}{\left(\ln\left(C\frac{8\pi^2\lambda_m T_m^2}{I_i}\right) - 2\ln\left(\frac{I}{R}\right)\right)^2} \tag{3.18}$$

$$r_0 = R\sqrt{\frac{\sigma_m}{C}} = R\sqrt{\frac{I}{R}}\sqrt[4]{\frac{I_i}{8\,\pi^2\lambda_m T_m^2\,C}} \tag{3.19}$$

Using the data reported in Table 3.1 it is possible to compute several parameters for the arc formed in the methane plasma, as shown in Figures 2.1.-1, 2, 3, 4 ,where

respectively are plotted the electric conductivity, the electric field, the radius of the plasma column and the discharge power per unit length.

The value of the constant C for the Saha Equation (3.8) in Table 2.1 is obtained from the expression:

$$C = 8300 * \exp\left(\frac{I_i^{Ar}}{I_i^{CH_4}}\right)$$

where the I_i are the ionization potential of Argon and methane, which have respectively the values of 72000 K and 132000 K [42].

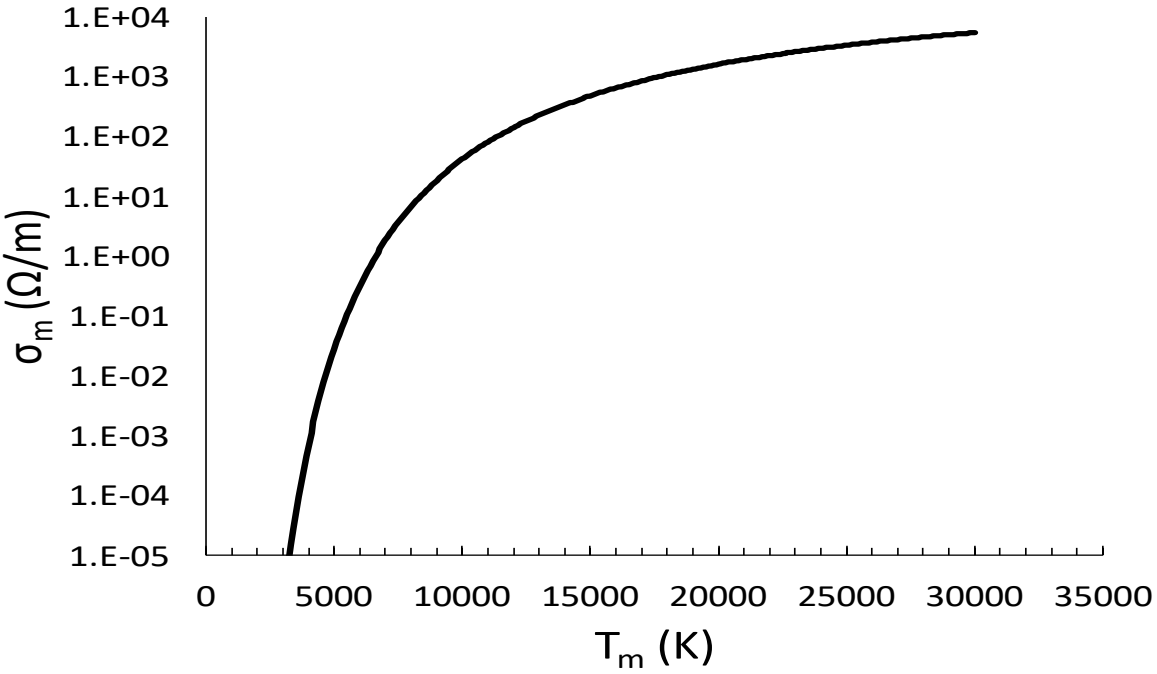

Figure 3.1.1: Electric conductivity of the arc in methane plasma as a function of the average temperature in the discharge.

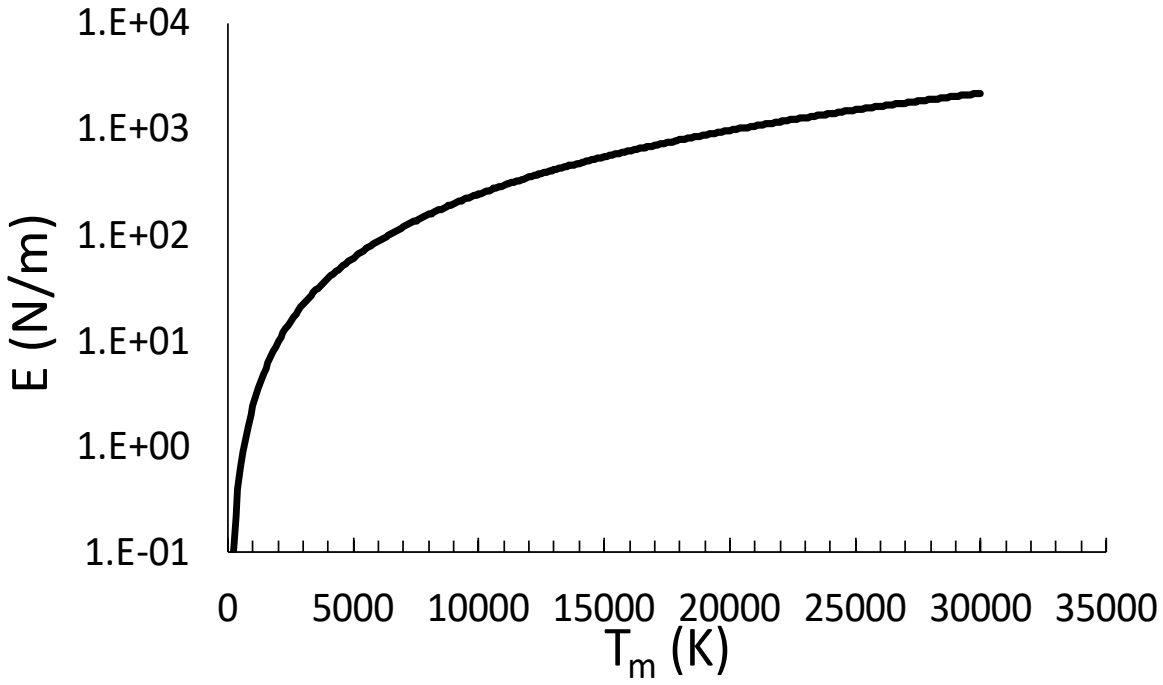

Figure 3.1.2: Electric field of the methane plasma arc as a function of the average temperature in the discharge.

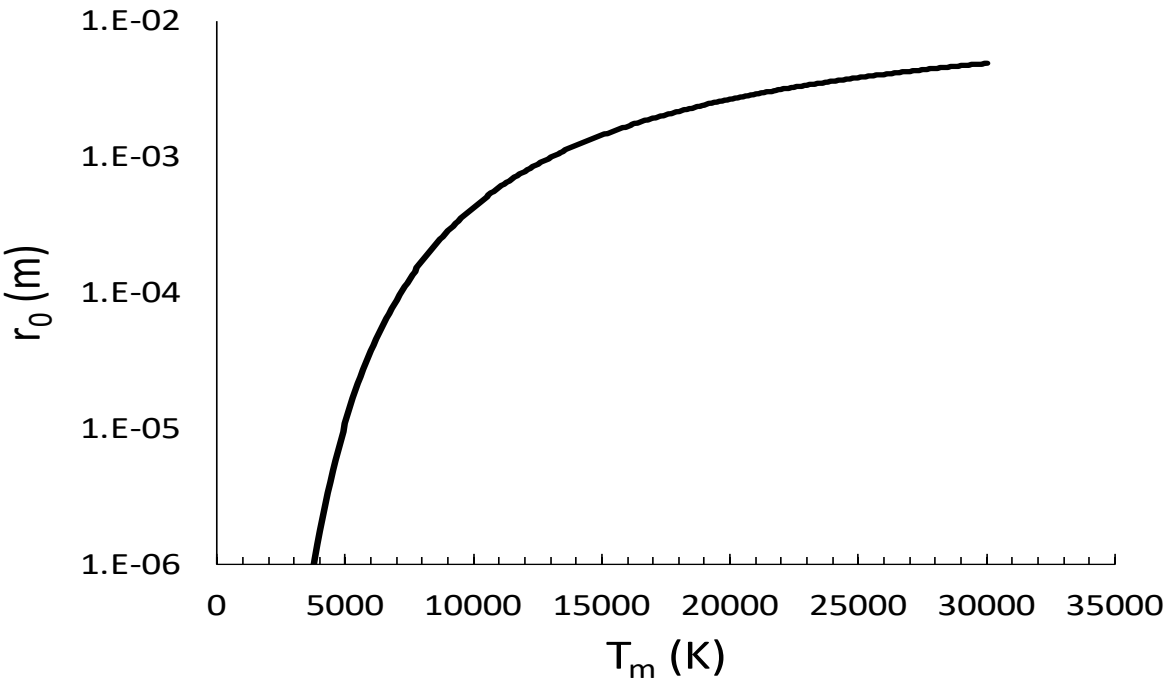

Figure 3.1.3: Radius of methane plasma arc column as a function of the average temperature in the discharge.

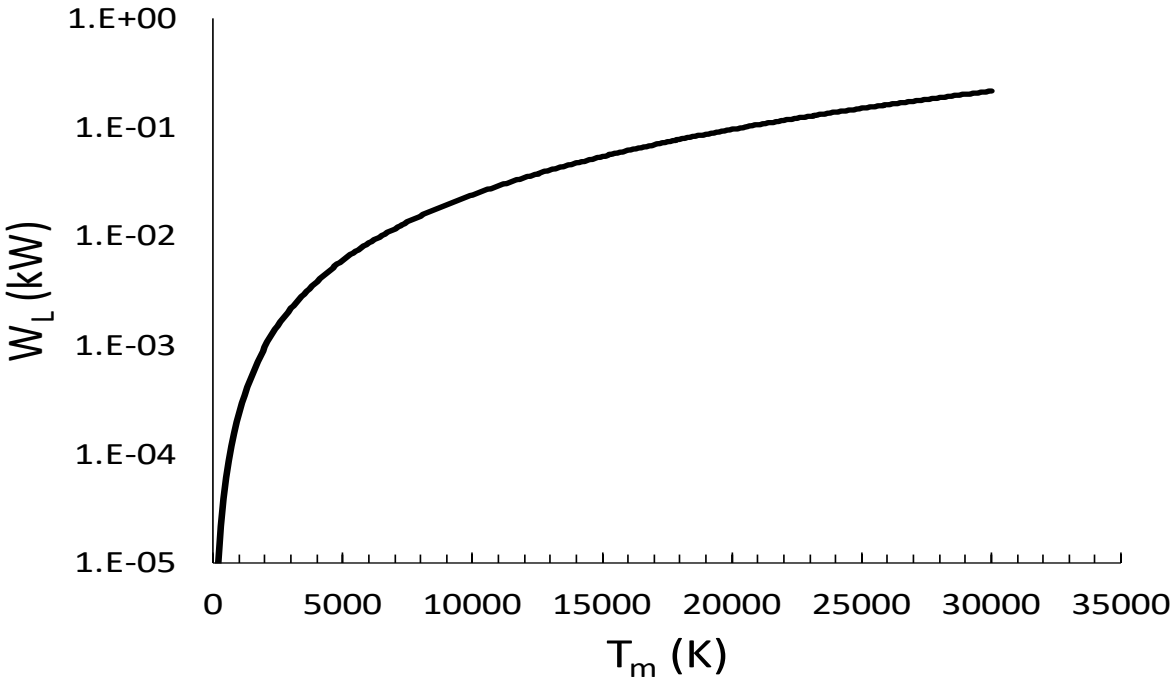

Figure 3.1.4: Discharge power per unit length of methane plasma arc as a function of the average temperature in the discharge.

For the specific system under consideration the calculated temperature, average electric field and discharge radius are reported in Table 2.2.

Table 3.1: Operating parameters of the case study.

Data					
C[39]	63349	Ω^{-1} m^{-1}	**I**[29]	100	A
Ii[42]	146333	K	λ_m [39]	0.14	W/m/K
	1.881	eV	**R**[29]	0.01651	m

Table 3.2: Operating parameters of the case study.

Results					
σ_m	995.61	Ω^{-1} m^{-1}	E	746.30	N/m
T_m	17618	K	r_0	0.00207	m
			W_L	0.075	kW/cm

Making some changes of the operating conditions, such as the current I and the chamber radius R, it is possible to observe the influence of these parameters on average temperature, electric conductivity, electric field, and discharge column radius.

In the following, three different cases are studied. The first one maintains the operative parameters unchanged except for the current which is doubled. In Table 2.3 all data are collected together with the calculated properties of the plasma discharge referring to the first case.

Table 3.3: First case about the variation of operating parameters in the plasma column.

Case 1		
Data		
$C_{[39]}$	63349	Ω^{-1} m^{-1}
$I_{i[42]}$	146333	K
I	20	A
$\lambda_{m[39]}$	0.14	W/m/K
R	0.01651	m
Results		
T_m	20311	K
σ_m	1727.11	Ω^{-1} m^{-1}
E	496	N/m
r_0	0.0027	m
W_L	0.0992	kW/cm

The second case conserves the original parameters with the exception of the chamber radius which is redoubled. All the data and calculated properties referring to this system are reported in Table 2.4.

Table 3.4: Second case about the variation of operating parameters in the plasma column.

Case 2		
Data		
$C_{[39]}$	63349	Ω^{-1} m^{-1}
$I_{i[42]}$	146333	K

I	10	A
$\lambda_{m[39]}$	0.14	W/m/K
R	0.03302	m
Results		
T_m	15506	K
σ_m	565.59	Ω^{-1} m^{-1}
E	578.14	N/m
r_0	0.0031	m
W_L	0.058	kW/cm

The last case does not preserve the original parameters, indeed both the current and the chamber radius are doubled. All the data and calculated properties referring to this system are reported in Table 2.5.

Table 3.5: Third case about the variation of operating parameters in the plasma column.

Case 3		
Data		
$C_{[39]}$	63349	Ω^{-1} m^{-1}
I_i	146333	K
I	20	A
λ_m	0.14	W/m/K
R	0.03302	m
Results		
T_m	17618	K

σ_m	995.61	Ω^{-1} m^{-1}
E	373.15	N/m
r_0	0.00414	m
W_L	0.0746	kW/cm

From the last case it is of interest to note that doubling both the current and the chamber radius, the average temperature and the electric conductivity of the plasma column remains unchanged with respect to the original conditions. This aspect follows from equation (3.15).

Besides, it is possible to develop the evolution of the medium temperature and the power as a function of the chamber radius R, as shown in Figure 2.1.5 and Figure 2.1.6. In Table 2.6 all the physical quantities of the methane arc plasma are reported in relation to the chamber radius, from which it is clear that the average temperature and so the discharge power decrease as the radius increases. In detail, a fixed arc length of 3 cm is chosen to compute the total power derived from the plasma generation.

Table 3.6: Methane arc plasma properties as a function of the chamber radius R

R (m)	**T_m (K)**	**σ_m (Ω^{-1} m^{-1})**	**E (N/m)**	**r_0 (m)**	**W_L (kW/cm)**	**W (kW)**
0.001	35631.45	8127.34	3052.76	0.00036	0.31	0.92
0.002	28855.28	5017.95	2002.06	0.00056	0.20	0.60
0.003	25845.32	3734.90	1606.16	0.00073	0.16	0.48
0.004	24024.09	3013.53	1387.78	0.00087	0.14	0.42
0.005	22760.32	2544.68	1245.61	0.00100	0.12	0.37
0.006	21812	2212.76	1143.97	0.00112	0.11	0.34
0.007	21063.35	1964.07	1066.79	0.00123	0.11	0.32

0.008	20450.91	1770.02	1005.66	0.00134	0.10	0.30
0.009	19936.52	1613.95	955.71	0.00144	0.10	0.29
0.01	19495.62	1485.40	913.90	0.00153	0.09	0.27
0.011	19111.58	1377.50	878.25	0.00162	0.09	0.26
0.012	18772.66	1285.51	847.38	0.00171	0.08	0.25
0.013	18470.29	1206.05	820.30	0.00179	0.08	0.25
0.014	18198.05	1136.66	796.30	0.00188	0.08	0.24
0.015	17951.03	1075.48	774.83	0.00195	0.08	0.23
0.016	17725.38	1021.10	755.47	0.00203	0.08	0.23
0.017	17518.03	972.41	737.90	0.00211	0.07	0.22
0.018	17326.51	928.53	721.85	0.00218	0.07	0.22
0.019	17148.81	888.78	707.12	0.00225	0.07	0.21
0.02	16983.25	852.57	693.53	0.00232	0.07	0.21

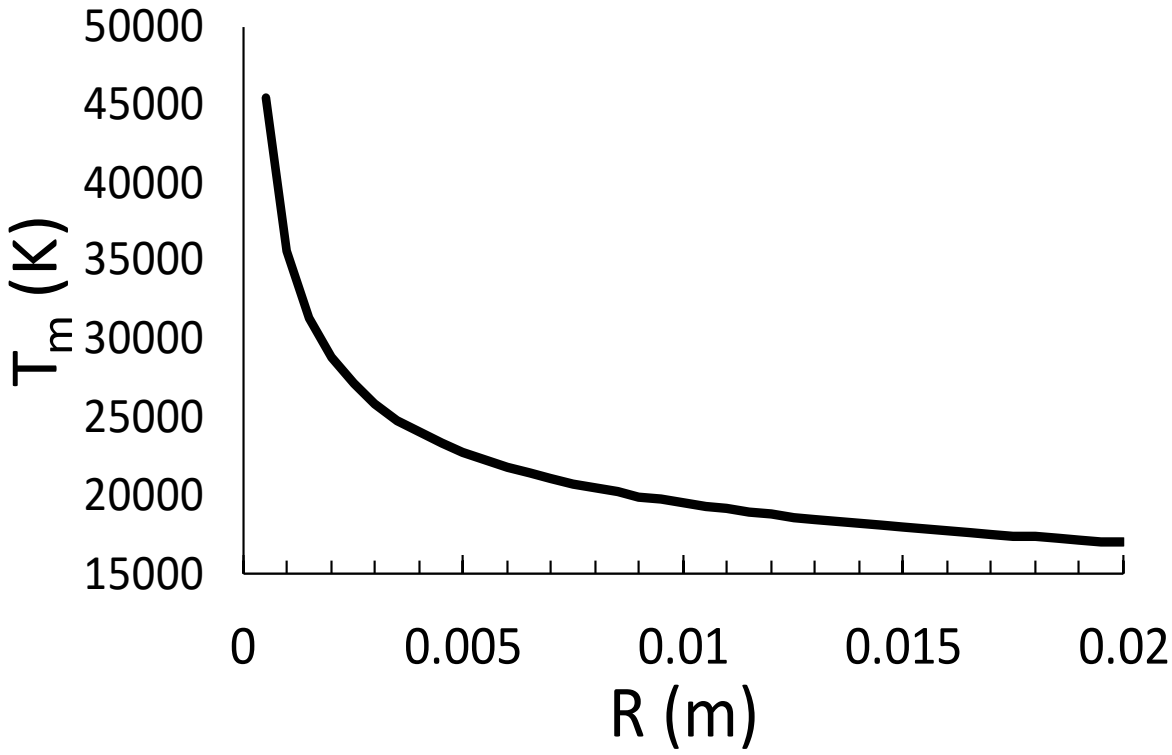

Figure 3.1.5: Average plasma temperature as a function of the chamber radius R

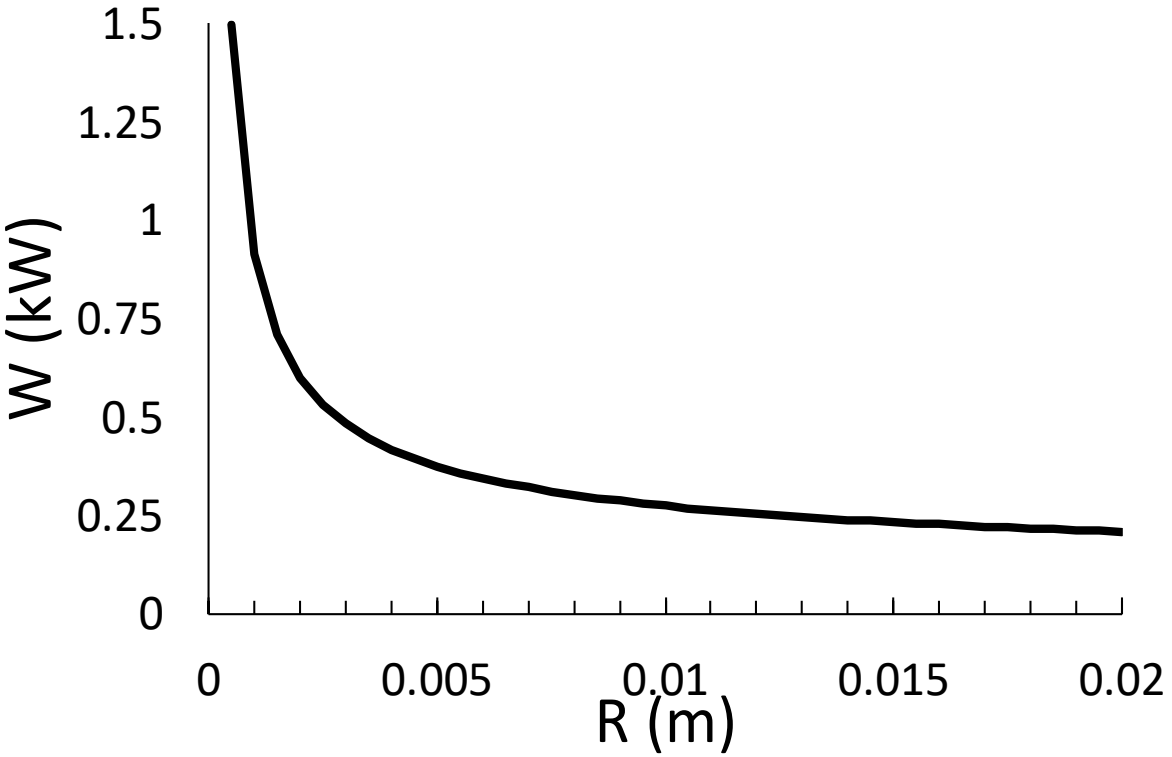

Figure 3.1.6: Average plasma temperature as a function of the chamber radius R

3.2. Results of an alternative model of a plasma discharge

Substituting the Saha equation in the Steenbeck-Raizer model [37, 38] using equation (3.26) it is possible to compute the average temperature of the arc plasma, its electric field, the column radius, and the discharge power per unit length.

In Table 3.7 all the data used for the computation are reported, and the corresponding results are reported in the Table 3.8.

Table 3.7: Data of an alternative model for the plasma discharge.

Data					
ε_0	8.854E-12	$s^4\ A^2\ m^{-3}\ kg^{-1}$	$R_{[29]}$	0.01651	m
I	10	A	**e**	-1.60218E-19	C
$\lambda_{[39]}$	0.14	W/m/K	$I_{i[42]}$	146332.9735	K
m_e	9.10938E-31	kg	$\hbar$	1.05457E-34	J*s
k_B	1.38065E-23	J/K	$\nu_{[43]}$	1E+23	s^{-1}
$n_{e[43]}$	1E+23	$1/m^3$			

Table 3.8: Results of an alternative model for the plasma discharge.

Results					
T_m	15642.5	K	Λ	79.17	-
C	229339	$\Omega^{-1}\ m^{-1}$	W_L	0.0589	kW/cm
σ_m	2134	$\Omega^{-1}\ m^{-1}$	**E**	588.35	N/m

ν_{eff}	2.32E+15	s^{-1}	r_0	0.0016	m
T_e	2.16E-19	eV			

In the Table 3.9 it is possible to see the differences occurring between the two models described in this chapter.

Table 3.9: Results comparison of the two different model.

Results					
$C_{[39]}$	8300	$\Omega^{-1}\ m^{-1}$	C	229339	$\Omega^{-1}\ m^{-1}$
T_m	21832	K	T_m	15642.5	K
E	1146.076	N/m	E	588.35	N/m
r_0	0.00309	m	r_0	0.0016	m
W_L	0.115	kW/cm	W_L	0.0589	kW/cm
σ_m	290.81	$\Omega^{-1}\ m^{-1}$	σ_m	2133.53	$\Omega^{-1}\ m^{-1}$

3.3. Results of the thermodynamic model

3.3.1. Results of the thermodynamic model (only gaseous phase)

In paragraph 2.1. the thermodynamics model of methane decomposition only considering the gaseous phase was described. Here the reported plots represent the result of that system at different conditions of pressure and temperature. In detail, first the system is investigated in the 1500-3000 °C range at four different pressures: 0.1, 1, 10 and 100 bar. Then, more specifically it was analyzed the equilibrium system at 1 bar from 3000 °C until 20000 °C.

In Figures 3.3.1, 2, 3, 4 are reported the equilibrium molar fractions computed at a different pressures, respectively 0.1, 1, 10 and 100 bar and at different temperatures in the 1500-3000 °C temperature range.

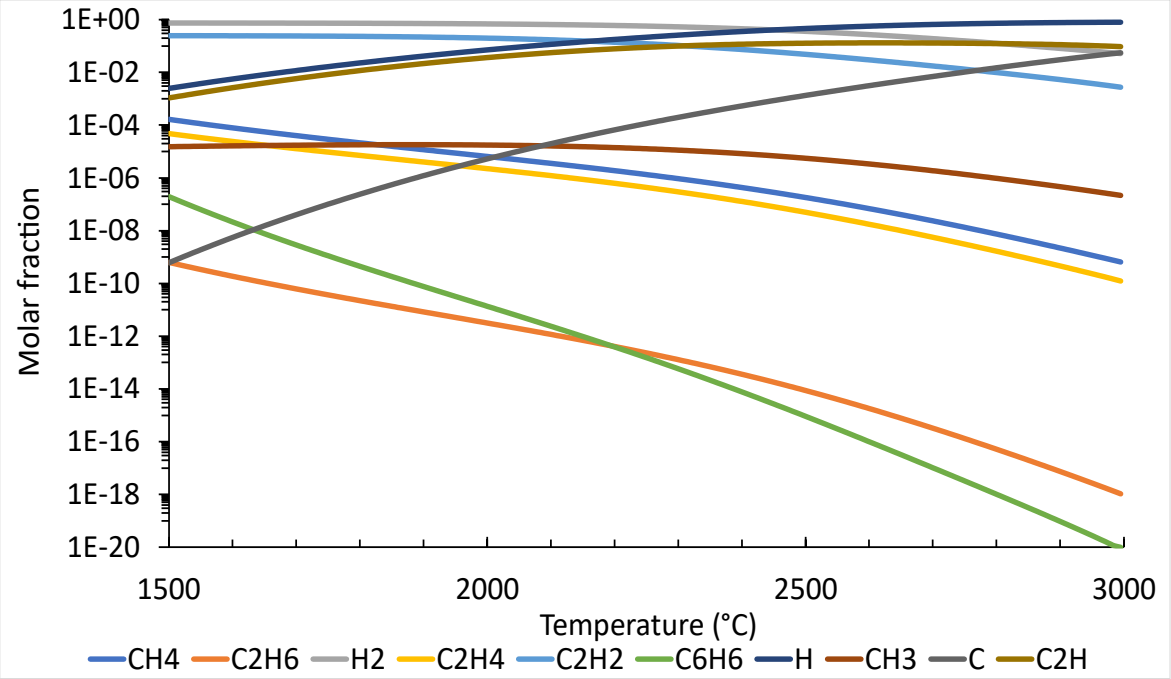

Figure 3.3.1 : Molar fraction at equilibrium conditions at 0.1 bar and in the 1500-3000 °C temperature range.

The most evident change along the different pressure condition is how the benzene and ethane decomposition decrease as the pressure is increased.

The second most interesting feature is the increase of species production from methane decomposition, which couples the pressure increase.

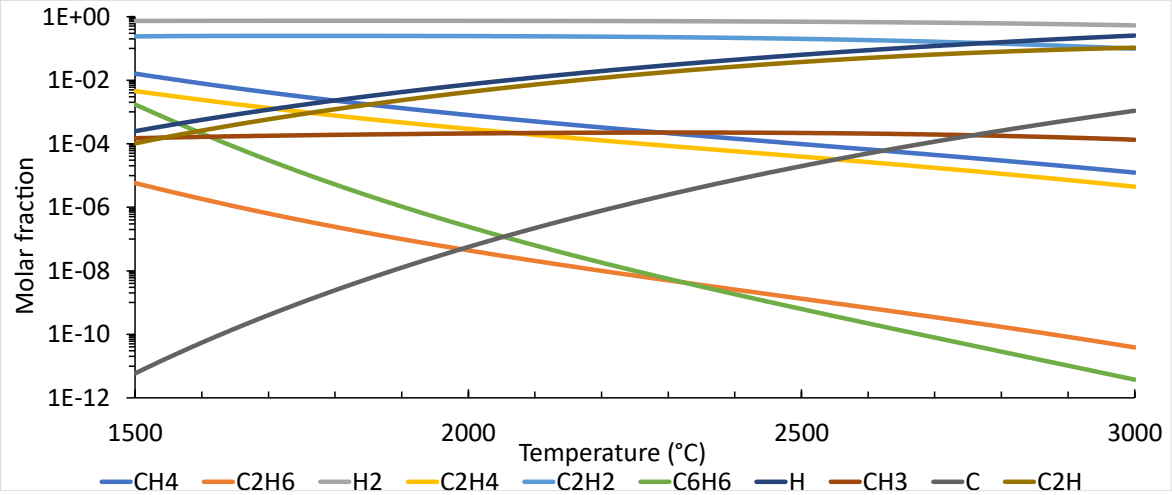

Figure 3.3.2: Molar fraction at equilibrium conditions at 1 bar and in the 1500-3000 °C temperature range.

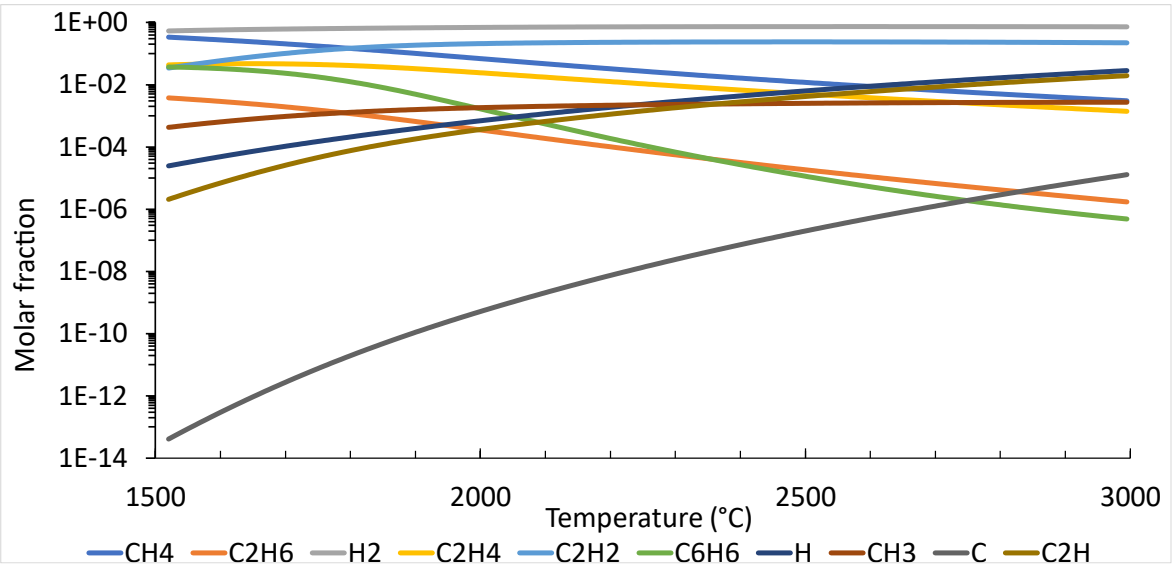

Figure 3.3.3. Molar fraction at equilibrium conditions at 10 bar and in the 1500-3000 °C temperature range.

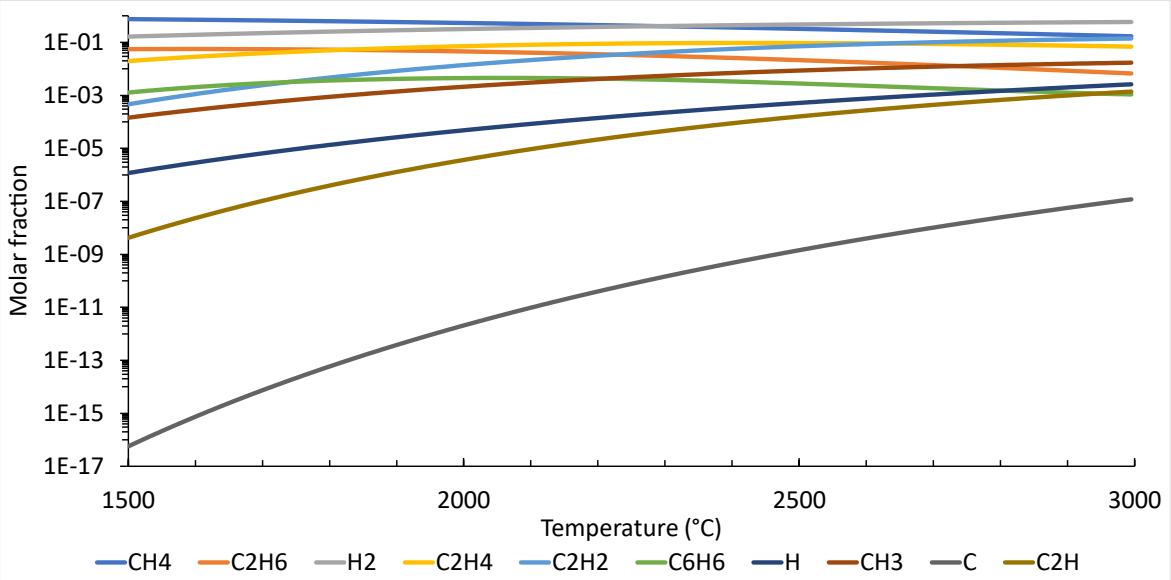

Figure 3.3.4: Molar fraction at equilibrium conditions at 100 bar and in the 1500-3000 °C temperature range.

In Figure 3.3.5 it is reported the equilibrium molar fraction of the system at 1 bar in the temperature range between 3000 and 6000 °C. It can be observed as ethane and benzene disappears almost totally. Also ethene, ethyne, methyl, ethynyl radical, and methane undergo a great decrease. The first three component are atomic carbon, atomic hydrogen, and molecular hydrogen.

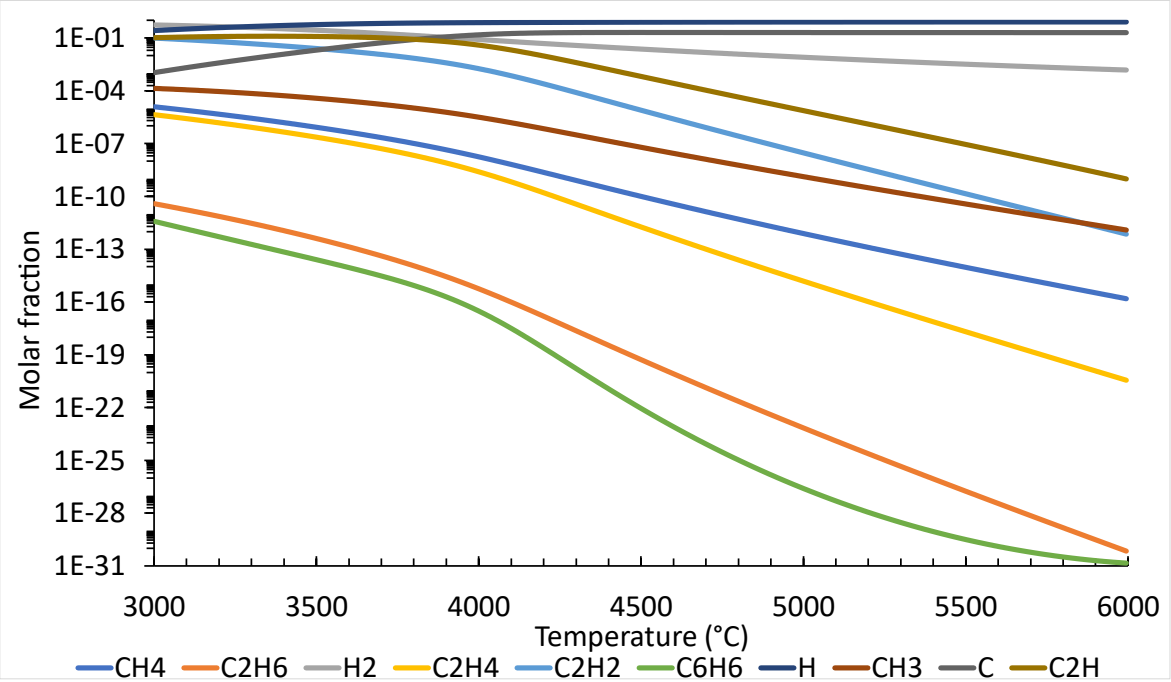

Figure 3.3.5: Molar fraction at equilibrium conditions at 1 bar and in the 3000-6000 °C temperature range.

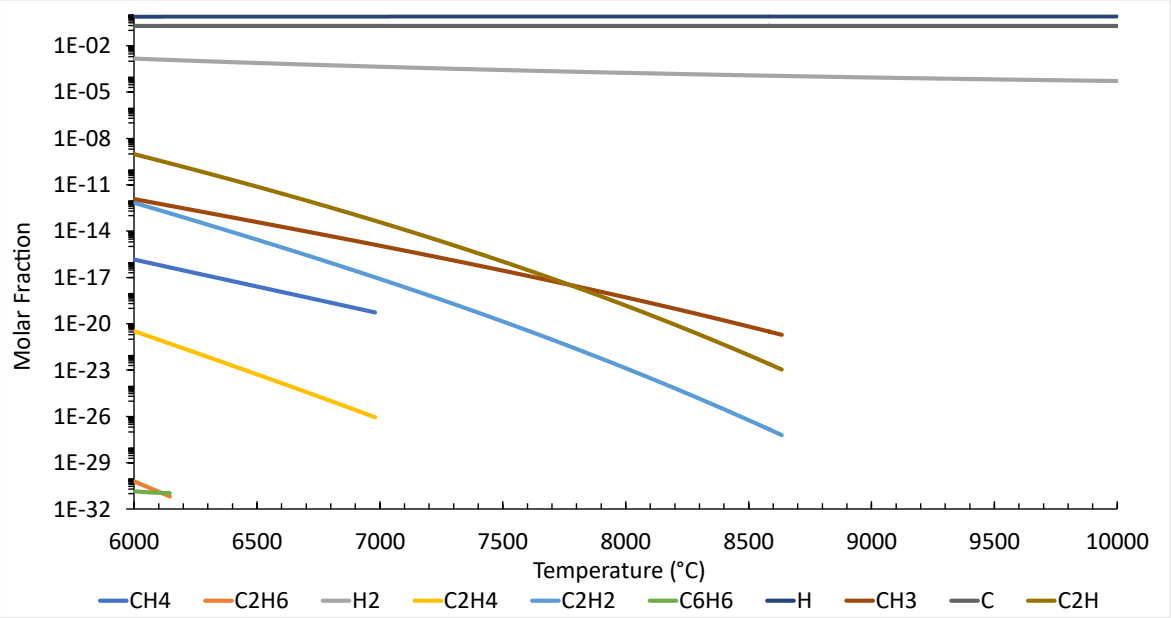

Figure 3.3.6: Molar fraction at equilibrium conditions at 1 bar and in the 6000-10000 °C temperature range.

In Figure 3.3.6 the equilibrium molar fraction of the system is depicted at 1 bar in the temperature range comprised between 6000 and 10000 °C.

It can be observed that ethane and benzene disappear just above the temperature of 6100 °C. Ethene and methane reach a too low concentration to be accounted for in the equilibrium calculation around the temperature of 7000 °C.

The same is found for ethyne, methyl, and the ethynyl radical, once the system reach the temperature of 8600 °C undergo a total decomposition. The first three components are atomic carbon, atomic hydrogen, and molecular hydrogen.

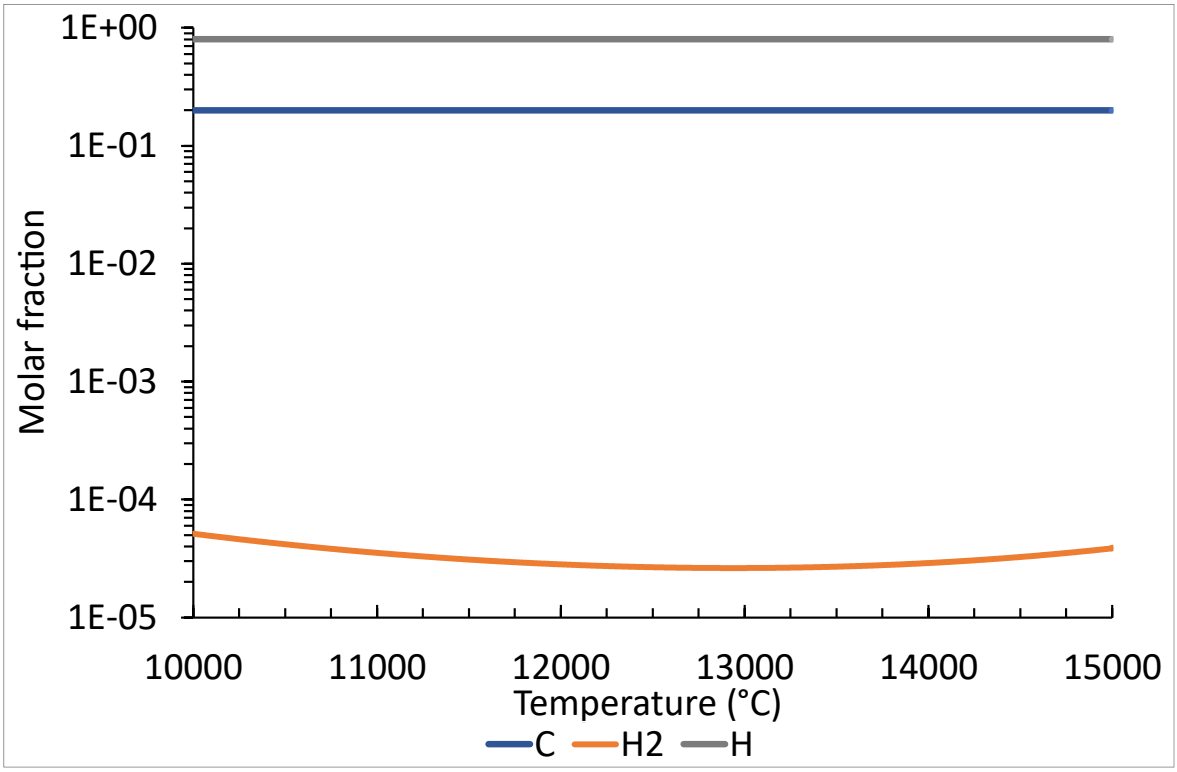

Figure 3.3.7: Molar fraction at equilibrium conditions at 1 bar and in the 10000-15000 °C temperature range.

In Figure 3.3.7 are reported the compositions at equilibrium at 1 bar and in the 10000-15000 °C temperature range. The unique three components are hydrogen, carbon, and hydrogen radical.

The molecular hydrogen curve has a particular shape, this is due to the fact that the specific heat is calculated in a different range of temperature.

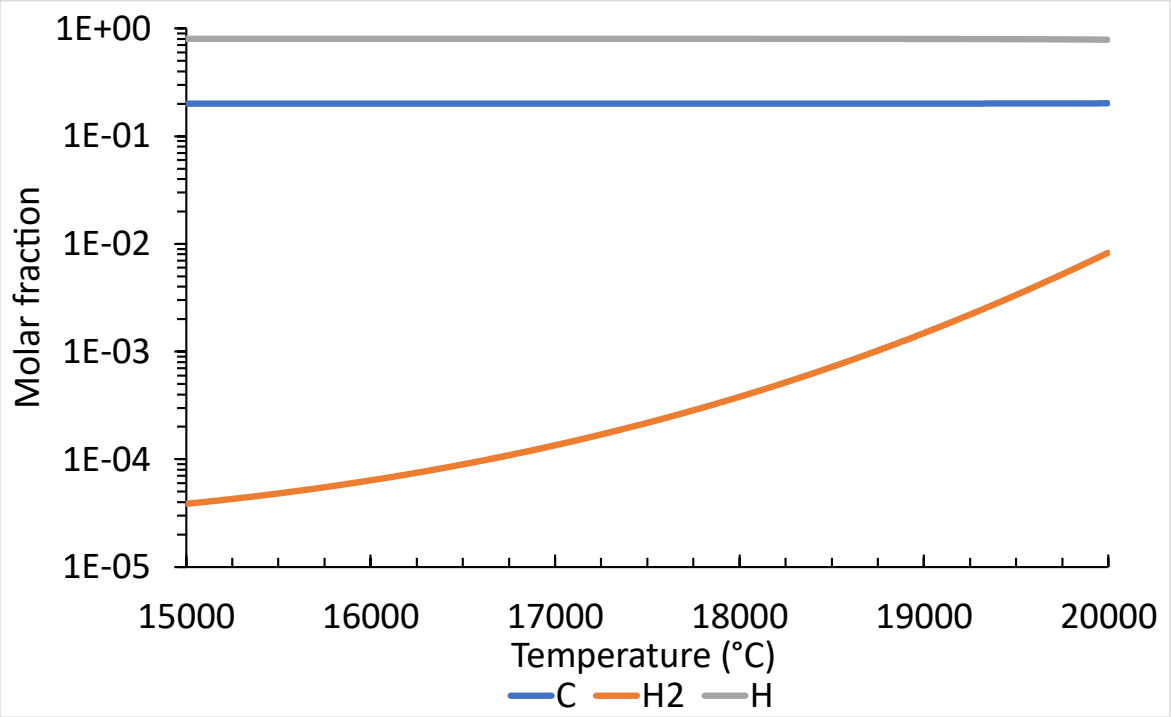

Figure 3.3.8: Molar fraction at equilibrium conditions at 1 bar and in the 15000-20000 °C temperature range.

In Figure 3.3.8 are reported the compositions at equilibrium at 1 bar and in the 15000-20000 °C temperature range. The unique three components are hydrogen, carbon, and hydrogen radical.

Of course the ratio between hydrogen and carbon radical is almost equal to four, while H_2 is present only in few traces.

The molecular hydrogen curve has a particular shape, this is due to the fact that the specific heat is calculated in a different range of temperature.

3.3.2. Results of the thermodynamics model (also considering the solid phase)

In paragraph 2.2. the thermodynamics model of methane decomposition obtained assuming solid carbon particles formation was described.

Here the reported plots represent the results of that system at different conditions of pressure (0.1, 1, 10, 50 and 100 bar) and dilution (0.5, 0.9 and 0.99 of molar fraction of the dilutant). The dilutant considered for the investigated system is the noble gas Argon.

All the charts shown in this section are obtained considering an initial mole of methane. The motive of this necessity is explained in paragraph 2.2.2.

The Figure 3.3.9 reports the compositions at equilibrium in the 0-6000 °C temperature range and at 0.1 bar. In these conditions the solid carbon formation is arrested around the temperature of 2700 °C.

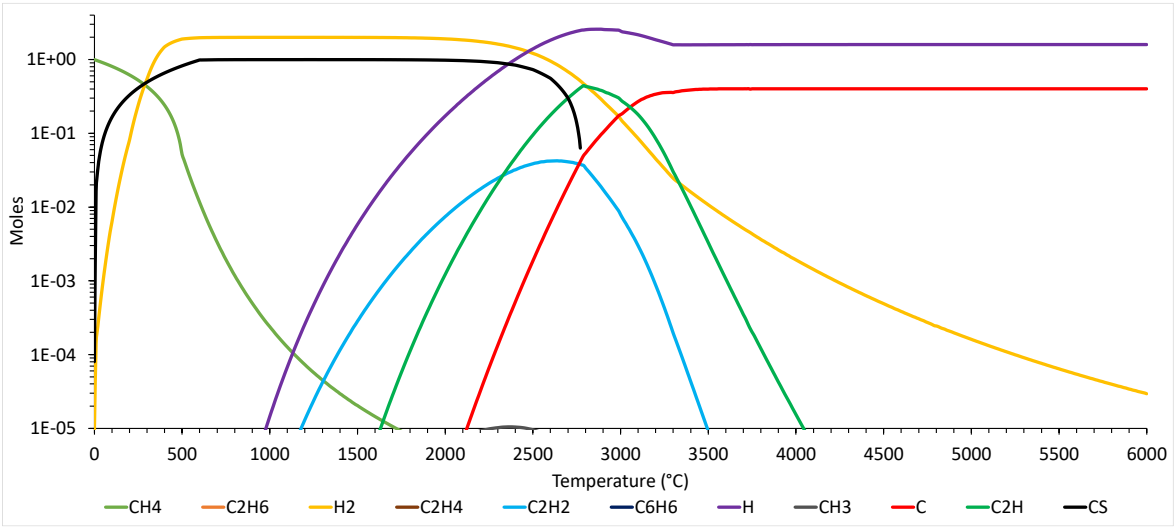

Figure 3.3.9: Equilibrium of a 1 mol of methane at 0.1 bar and in the 0-6000 °C temperature range.

The Figure 3.3.10 reports the compositions at equilibrium in the 0-6000 °C temperature range and at 1 bar. In these conditions the solid carbon formation is arrested around the temperature of 3100 °C.

An evident difference with the previous chart is the proximity of the two peaks of ethyne and ethynyl radical. Other two differences are the growth of methyl radical and the appearance of ethene.

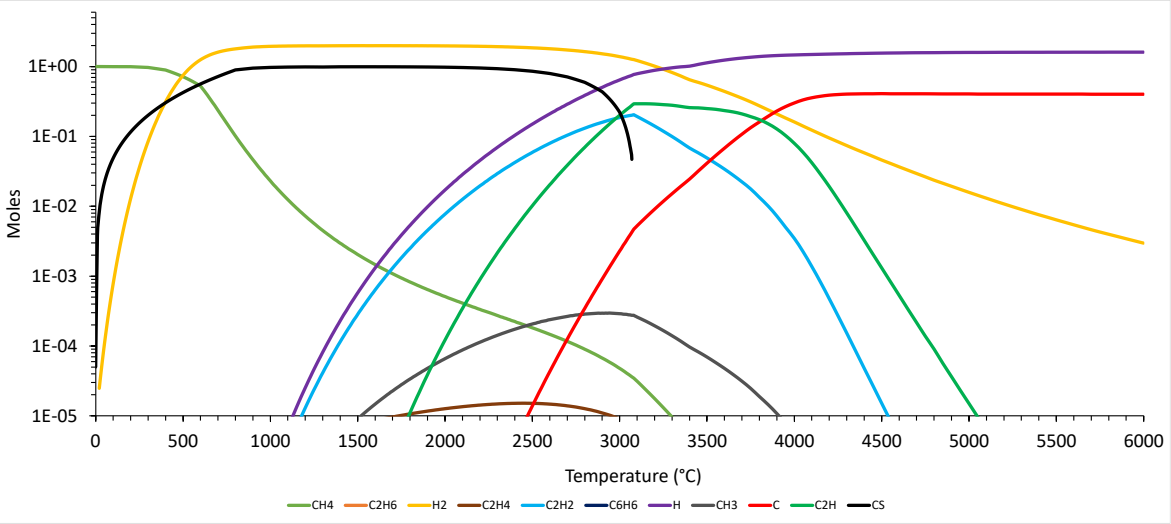

Figure 3.3.10: Equilibrium of a 1 mol of methane at 1 bar and in the 0-6000 °C temperature range.

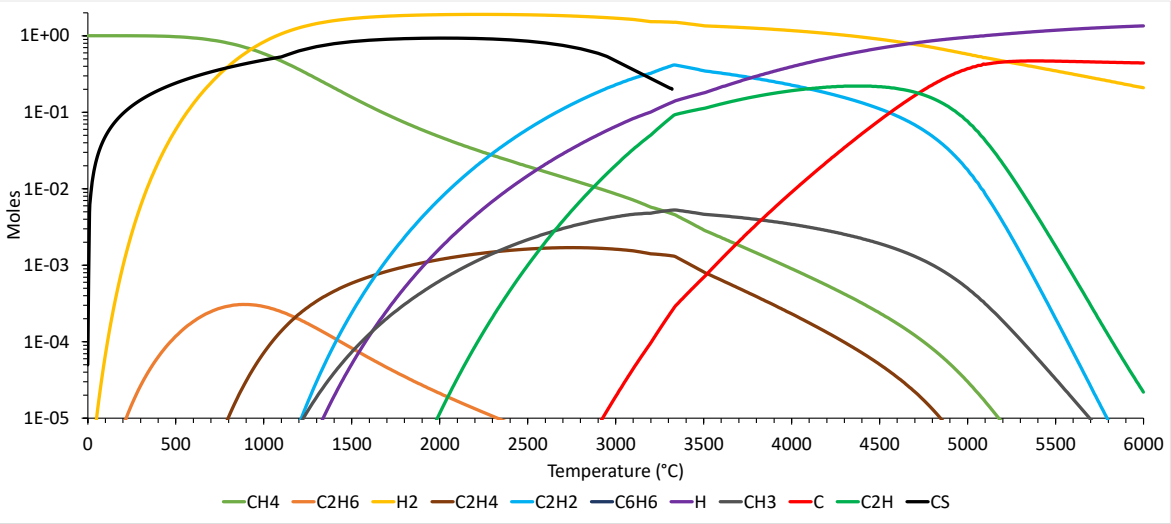

Figure 3.3.11: Equilibrium of a 1 mol of methane at 10 bar and in the 0-6000 °C temperature range.

In Figure 3.3.11 are reported the compositions at equilibrium in the 0-6000 °C temperature range and at 10 bar. In these conditions the solid carbon formation is arrested around the temperature of 3400 °C.

At the temperature of 3400 °C the peak of ethyne curve overlook the ethynyl radical one. With respect to the Figure 3.3.10 there is also the appearance of ethane.

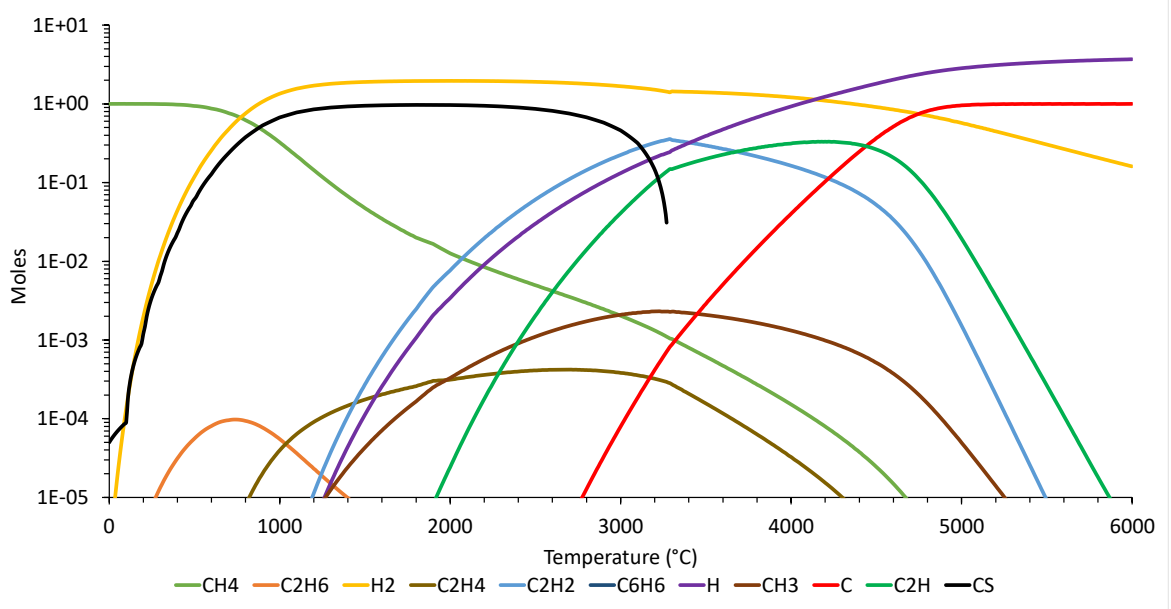

Figure 3.3.12: Equilibrium of a 1 mol of methane at 50 bar and in the 0-6000 °C temperature range.

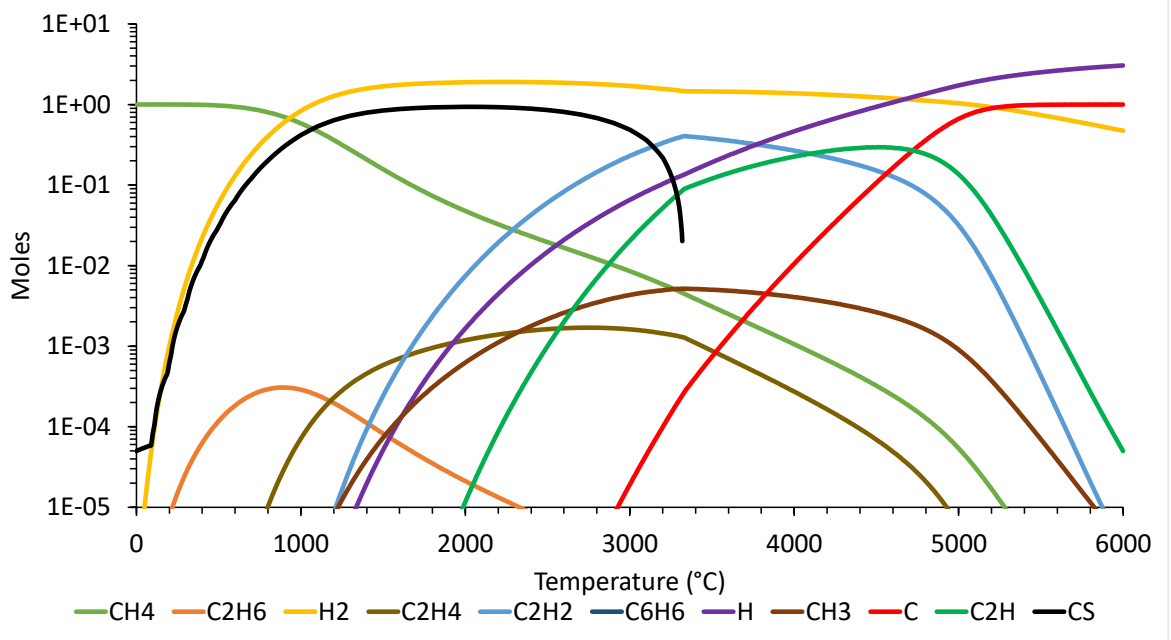

Figure 3.3.13: Equilibrium of a 1 mol of methane at 100 bar and in the 0-6000 °C temperature range.

In Figure 3.3.12 and 3.3.13 the compositions at equilibrium are depicted respectively at a pressure of 50 and 100 bar in the 0-6000 °C temperature range. For both conditions, the solid carbon formation is arrested around the temperature of 3200 °C.

It is of great interest to investigate the equilibrium composition at 1 bar in a dilute system, in these cases with Argon.

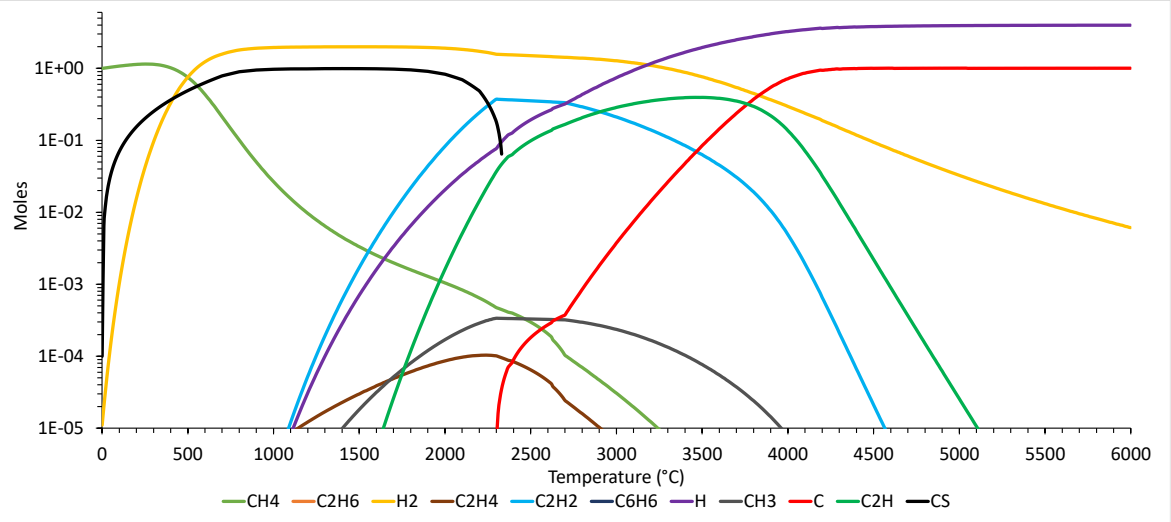

Figure 3.3.14: Equilibrium of a 1 mol of methane in a diluted system with Argon, whose molar fraction is 0.5, at 1 bar and in the 0-6000 °C temperature range.

In Figure 3.3.14 the compositions at equilibrium in the 0-6000 °C temperature range and diluted with 0.5 of Argon are reported. In these condition the solid carbon formation is arrested around the temperature of 2400 °C, which is a temperature lower than in the concentrated system.

As compared to the pure system at 1 bar, ethene has a higher concentration in range in which it is present, and the ethyne peak is above the ethynyl curve.

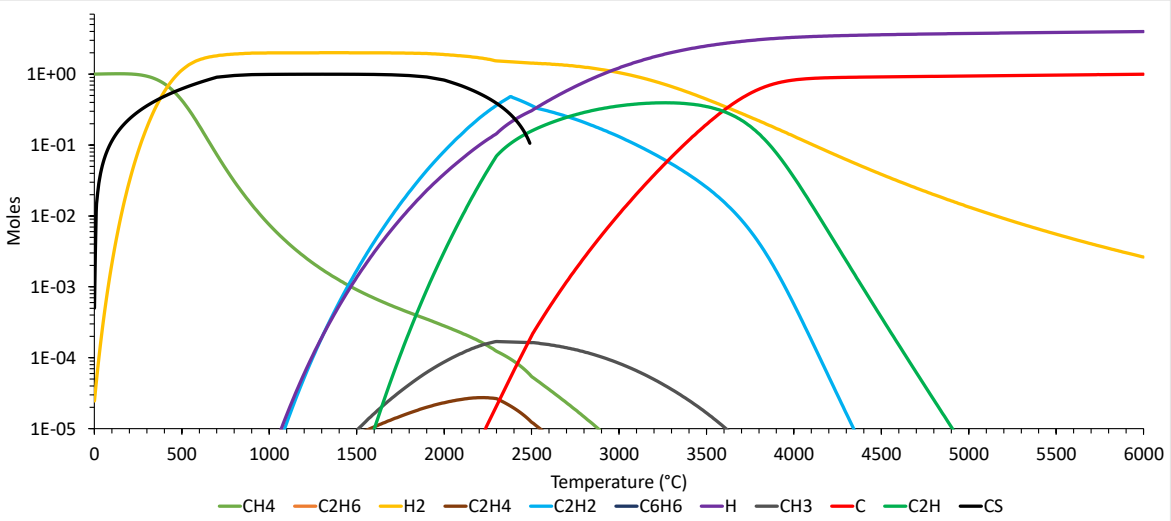

Figure 3.3.15: Equilibrium of a 1 mol of methane in a diluted system with Argon, whose molar fraction is 0.9, at 1 bar and in the 0-6000 °C temperature range.

In Figure 3.3.15 the compositions at equilibrium in the 0-6000 °C temperature range and diluted with 0.9 of Argon are reported. In these conditions the solid carbon formation is arrested around the temperature of 2500 °C, which is still a temperature lower than found for the pure system.

As compared to the pure system at 1 bar, ethene has a slightly higher concentration in the range in which is present. The ethyne peak is above the ethynyl curve.

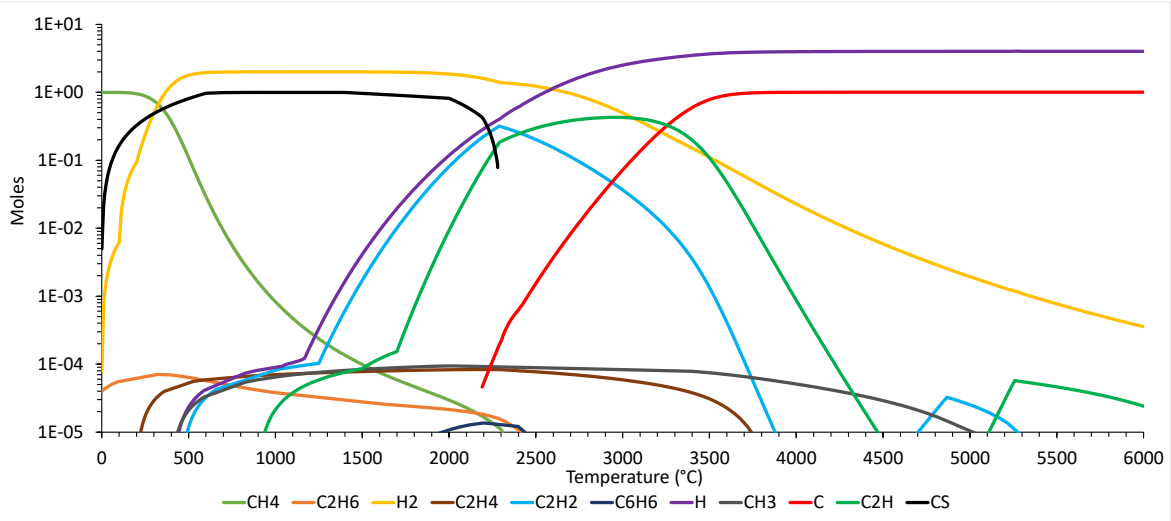

Figure 3.3.16: Equilibrium of a 1 mol of methane in a diluted system with Argon, whose molar fraction is 0.99, at 1 bar and in the 0-6000 °C temperature range.

In Figure 3.3.16 the compositions at equilibrium in the 0-6000 °C temperature range and diluted with 0.99 of Argon are reported. In these conditions the solid carbon

formation is arrested around the temperature of 2300 °C, which is yet a temperature lower than one in pure system.

As compared to the pure system at 1 bar, a different behavior of curve is observed in the 0-1500 °C temperature range. Ethane is present up to 2500 °C, while ethene and methyl radical have significantly extended their existence windows.

For the first time the benzene overcomes the value of 1E-05 in the 2000-2500°C temperature range.

3.4. Results of kinetic simulations

The simulations have been performed with OpenSMOKE++ Suite [40, 41] for the two different reactor configurations described by Fincke [29].

A fundamental parameter required for the simulations is the inlet temperature at the reactor section. This temperature is calculated through the energy balance upon the mixing between the bypass flow rate and the discharge plasma flow rate.

After the calculations about the temperature are completed, the inlet conditions of the two different cases are reported in Tables 3.10 and 3.11, which correspond to the two experimental reference cases considered.

Table 3.10: Inlet conditions of the first experimental setup considered [29].

Data			
Molar flow rate [mol/s]	0.275	**C2H2 molar fraction [-]**	0.197
Temperature [K]	2683	**CH3 molar fraction [-]**	0.0001
Pressure [bar]	0.85	**Ar molar fraction [-]**	0.2305
H2 molar fraction [-]	0.48	**H molar fraction [-]**	0.0499
C2H molar fraction [-]	0.0425		

Table 3.11: Inlet conditions of the first experimental setup considered [29].

Data			
Molar flow rate [mol/s]	0.20	**C2H2 molar fraction [-]**	0.0365

Temperature [K]	3433	**C molar fraction [-]**	0.0055
Pressure [bar]	0.771	**Ar molar fraction [-]**	0.303
H2 molar fraction [-]	0.211	**H molar fraction [-]**	0.315
C2H molar fraction [-]	0.129		

Initially the simulations were performed using the original reactor dimension. The simulations performed in the considered conditions showed that the formation of soot is minor, while acetylene is main product. This is in agreement with experimental evidences which showed that the formation of carbon in the explored conditions is smaller than a few percent, in mole fraction terms.

In order to investigate whether a modification of the reactor may enhance the conversion to carbon the impact of different reactor parameters on the system evolution was investigated. The most sensitive parameters are those controlling the residence time: the reactor length (which was increased up to one meter) and the diameter. As the velocity inside the reactor is reduced, and residence time increases sufficiently to trigger the formation of the soot precursors and the consequent soot formation. In particular, simulations were performed increasing the radius of the reactor by one time and half, and two times and half the original dimension reported in Fincke [29] experience (0.0254 m).

To investigate properly the response of the system, different temperature profiles are imposed, by fixing the temperature at 10 cm from the reactor inlet and assuming a linear profile. The simulations were performed using two different 10 cm temperatures: 1500 K and 1900 K.

Besides, three different final temperatures are considered: 300 K, 800 K, and 1300 K.

In Figure 3.4.1 and 3.4.2, the hydrogen molar fraction profile and the temperature are depicted respectively. In the chart legend the parameter TF indicates the final temperature, PT the temperature imposed at 10 cm, and Rx how many times the radius is increased.

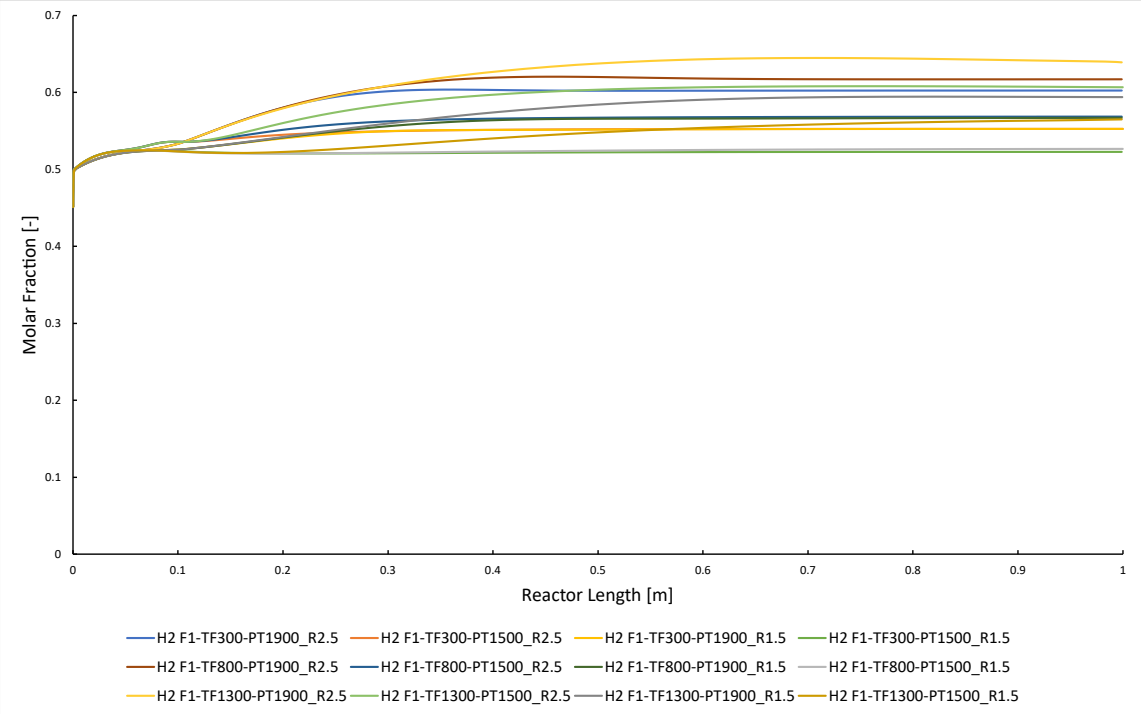

Figure 3.4.1: Hydrogen molar fraction profile at different conditions based on first Fincke setup.

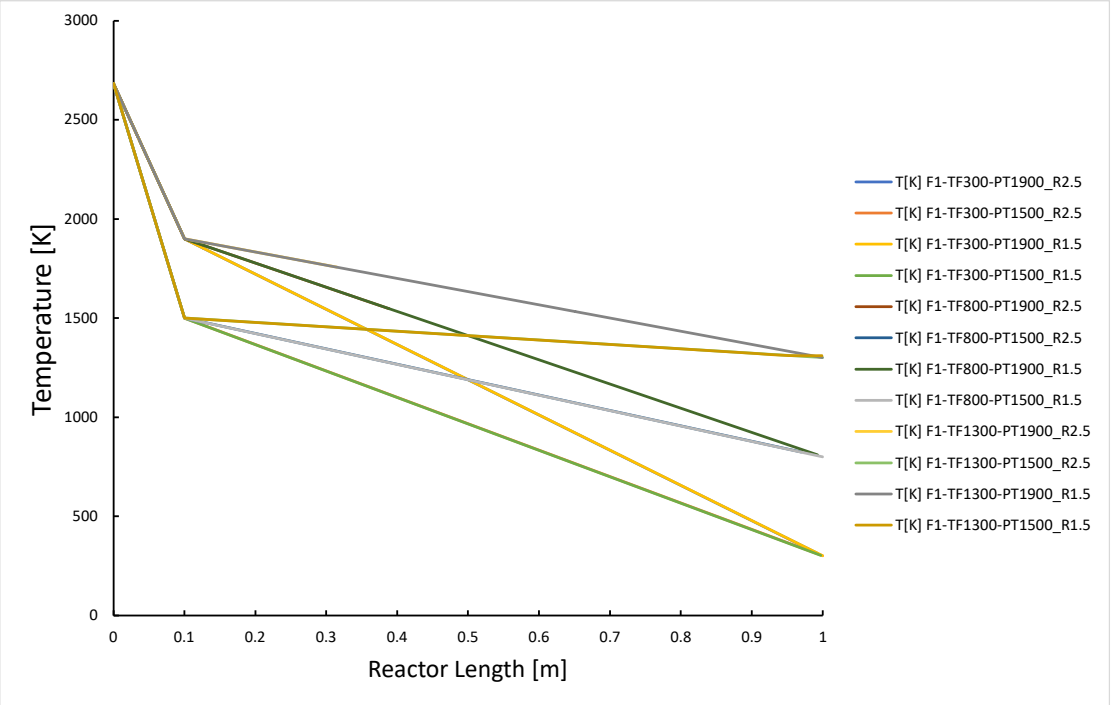

Figure 3.4.2: Temperature profile at different conditions based on first Fincke setup.

The results of interests are hydrogen, acetylene and BIN25CJ (the most present soot component) production. Thus, in this section are reported the massive fractions of H_2, C_2H_2, and BIN25CJ, and also the hydrogen molar fraction.

The results are reported depending on the final temperature in Tables 3.12, 13, 14. The relative values corresponds to the case of a final temperature of 300-800-1300 K, respectively.

As evidenced from the data obtained from the simulations, when the radius is increased 2.5 times, the soot and hydrogen production reaches the maximum. This happens since the velocity in the reactor is significantly reduced, so that the residence time is enough to guarantee the proper acetylene conversion. Another aspect that influences the results is the value of the temperature imposed at 10 cm from inlet section of the PFR. Imposing a temperature of 1900 K, the time in which the species are in a temperature interval favorable for soot formation is maximized.

Table 3.12: Results from simulations of first Fincke setup with a final temperature of 300 K.

	Case PT 1500 R 1.5	**Case PT 1900 R 1.5**	**Case PT 1500 R 2.5**	**Case PT 1900 R 2.5**
C_2H_2 massive fraction [-]	2.27E-01	2.02E-01	1.35E-01	1.06E-01
BIN25CJ massive fraction [-]	7.81E-03	5.94E-02	7.32E-02	1.62E-01
H_2 massive fraction [-]	5.73E-02	6.12E-02	5.86E-02	6.56E-02
H_2 molar fraction [-]	5.23E-01	5.52E-01	5.53E-01	6.02E-01

Table 3.13: Results from simulations of first Fincke setup with a final temperature of 800 K.

	Case PT 1500 R 1.5	**Case PT 1900 R 1.5**	**Case PT 1500 R 2.5**	**Case PT 1900 R 2.5**
C_2H_2 massive fraction [-]	1.96E-01	1.71E-01	8.92E-02	7.89E-02
BIN25CJ massive fraction [-]	1.56E-02	8.85E-02	1.13E-01	1.90E-01
H_2 massive fraction [-]	5.68E-02	6.24E-02	5.94E-02	6.69E-02
H_2 molar fraction [-]	5.27E-01	5.67E-01	5.69E-01	6.17E-01

Table 3.14: Results from simulations of first Fincke setup with a final temperature of 1300 K.

	Case PT 1500 R 1.5	**Case PT 1900 R 1.5**	**Case PT 1500 R 2.5**	**Case PT 1900 R 2.5**
C_2H_2 massive fraction [-]	1.29E-01	1.36E-01	5.02E-02	6.28E-02
BIN25CJ massive fraction [-]	8.13E-02	1.29E-01	1.95E-01	2.22E-01
H_2 massive fraction [-]	6.03E-02	6.55E-02	6.43E-02	7.02E-02
H_2 molar fraction [-]	5.64E-01	5.94E-01	6.07E-01	6.40E-01

In Figure 3.4.3 and 3.4.4, the temperature and the hydrogen molar fraction profiles are depicted, respectively. In the chart legend the parameter TF indicates the final temperature, PT the temperature imposed at 10 cm, and Rx how many times the radius is increased. As compared to Fig. 3.4.2, in Fig. 3.4.4 the hydrogen molar fractions is always lower, since in the first series of cases the initial molar fraction is higher than the ones in the second series.

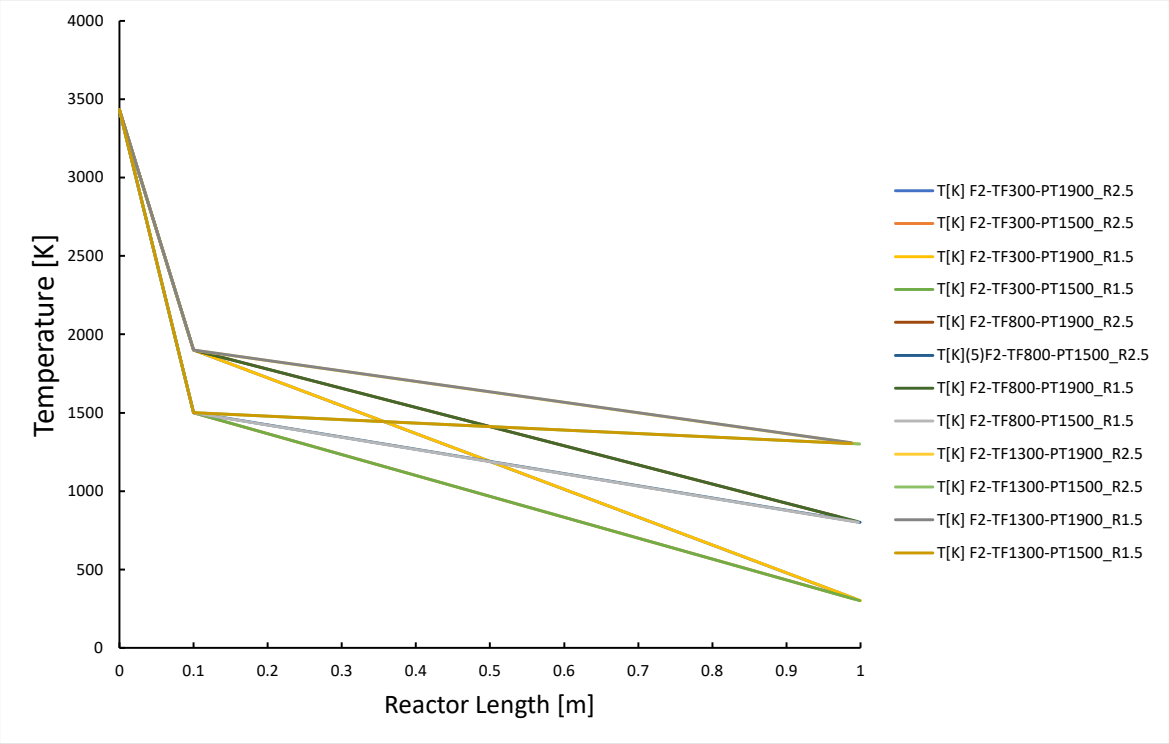

Figure 3.4.3: Temperature profile at different conditions based on second Fincke setup.

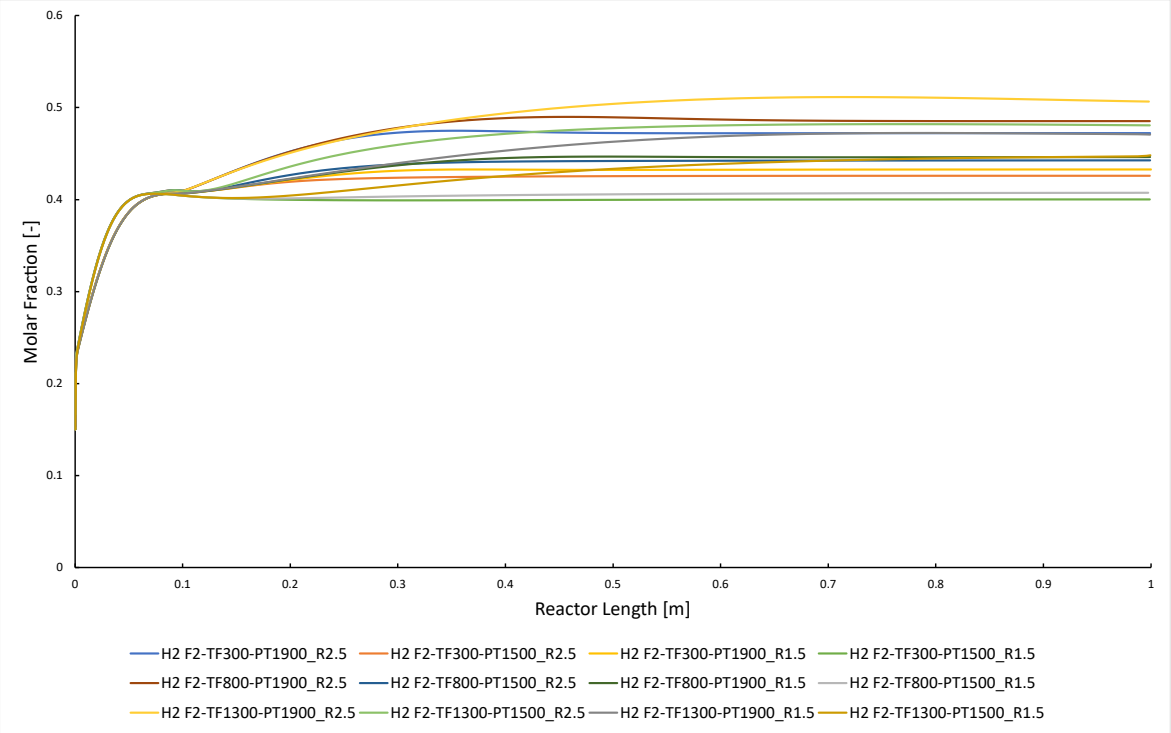

Figure 3.4.4: Hydrogen molar fraction profile at different conditions based on second Fincke setup.

The results of our interests are relative to the hydrogen, acetylene and BIN25CJ (which is the most present soot component) production. So that in this section are reported the massive fractions of H_2, C_2H_2, and BIN25CJ, and also the hydrogen molar fraction.

Here below the results are reported depending on the final temperature, in Tables 3.15, 16, 17 the relative values correspond respectability to the case of a final temperature of 300 K, 800 K, and 1300 K.

The data obtained from the simulations suggest that, when the radius is increased 2.5 times, the soot and hydrogen production reaches the peak values. This is due to the fact that the velocity inside the reactor is significantly reduced, as a consequence the residence time results enough to guarantee an adequate acetylene conversion. A second aspect that influences the results is the value of the temperature imposed at 10 cm from the inlet section of the PFR. Imposing a temperature of 1900 K, the time in which the species are in a temperature interval favorable for soot formation is long enough to give the possibility to acetylene to form soot precursor and then the soot.

Table 3.15: Results from simulations of second experimental setup with a final temperature of 300 K.

	Case PT 1500 R 1.5	**Case PT 1900 R 1.5**	**Case PT 1500 R 2.5**	**Case PT 1900 R 2.5**
C_2H_2 massive fraction [-]	1.56E-01	1.34E-01	9.71E-02	7.64E-02
BIN25CJ massive fraction [-]	4.57E-03	4.92E-02	5.02E-02	1.12E-01
H_2 massive fraction [-]	3.46E-02	3.78E-02	3.59E-02	4.07E-02
H_2 molar fraction [-]	4.00E-01	4.33E-01	4.26E-01	4.72E-01

Table 3.16: Results from simulations of second experimental setup with a final temperature of 800 K.

	Case PT 1500 R 1.5	**Case PT 1900 R 1.5**	**Case PT 1500 R 2.5**	**Case PT 1900 R 2.5**
C_2H_2 massive fraction [-]	1.29E-01	1.13E-01	6.58E-02	5.78E-02
BIN25CJ massive fraction [-]	1.73E-02	7.01E-02	8.16E-02	1.31E-01
H_2 massive fraction [-]	3.47E-02	3.87E-02	3.70E-02	4.18E-02
H_2 molar fraction [-]	4.07E-01	4.46E-01	4.43E-01	4.85E-01

Table 3.17: Results from simulations of second experimental setup with a final temperature of 1300 K.

	Case PT 1500 R 1.5	**Case PT 1900 R 1.5**	**Case PT 1500 R 2.5**	**Case PT 1900 R 2.5**
C_2H_2 massive fraction [-]	8.42E-02	9.15E-02	3.85E-02	4.57E-02
BIN25CJ massive fraction [-]	7.34E-02	9.73E-02	1.39E-01	1.53E-01
H_2 massive fraction [-]	3.81E-02	4.10E-02	4.08E-02	4.39E-02
H_2 molar fraction [-]	4.47E-01	4.71E-01	4.81E-01	5.07E-01

4 Conclusion and future developments

The subject of this thesis has been the study of a thermal plasma methane decomposition process where the power is delivered by an arc discharge and the purpose of the process is to decompose methane into hydrogen and carbon.

The results indicate that the investigated system is suitable for hydrogen production, but that there is room for performance improvement.

For example, if the pressure of the system is increased to 10 bar, the temperature window for the formation of solid carbon would increase from 3000 °C to 3400 °C, thus having a positive impact on the system performances as it would reduce acetylene production.

Two others parameter that play a key role are the dimensions of the reactor and the temperature profile.

It is evidenced that if the reactor was elongated, leading to a reduction of the velocity and to an increase of the residence time, the soot precursor reactions would be favored.

The temperature profile also plays a key role. The 1300-1900 K temperature range results very favorable to soot formation, hence the best strategy is to drastically cool down the reactor as fast as possible. So that for most of the reactor the conditions will lead to a consistent hydrogen and soot production, limiting acetylene formation.

Future improvements could consist in the development of a thermal plasma reactor that is able to work at a higher pressure to allow a massive production of solid carbon also at higher temperature than the temperatures derived in the thermodynamic equilibrium analysis. An interesting aspect that may be deepened is the research of the best performing temperature profile. Its role has been demonstrated to be important as it allowed to highlight both the relevance of the initial reactions leading to soot formation as well as since its strong impact on the extent of the maximum hydrogen production.

Bibliography

[1] IPCC, 2022: *Climate Change 2022: Impacts, Adaptation, and Vulnerability.* Contribution of Working Group II to the Sixth Assessment Report of the Intergovernmental Panel on Climate Change [H.-O. Pörtner, D.C. Roberts, M. Tignor, E.S. Poloczanska, K. Mintenbeck, A. Alegría, M. Craig, S. Langsdorf, S. Löschke, V. Möller, A. Okem, B. Rama (eds.)]. Cambridge University Press. Cambridge University Press, Cambridge, UK and New York, NY, USA, 3056 pp., doi:10.1017/9781009325844.

[2] IPCC, 2018: Global warming of 1.5°C. An IPCC Special Report on the impacts of global warming of 1.5°C above pre-industrial levels and related global greenhouse gas emission pathways, in the context of strengthening the global response to the threat of climate change, sustainable development, and efforts to eradicate poverty [V. Masson-Delmotte, P. Zhai, H. O. Pörtner, D. Roberts, J. Skea, P.R. Shukla, A. Pirani, W. Moufouma-Okia, C. Péan, R. Pidcock, S. Connors, J. B. R. Matthews, Y. Chen, X. Zhou, M. I. Gomis, E. Lonnoy, T. Maycock, M. Tignor, T. Waterfield (eds.)].

[3] Hannah Ritchie, Max Roser and Pablo Rosado (2020) - "CO_2 and Greenhouse Gas Emissions". Published online at OurWorldInData.org. Retrieved from: "https://ourworldindata.org/co2-and-other-greenhouse-gas-emissions"

[4] IPCC, 2022*:* Climate Change 2022: Mitigation of Climate Change. Contribution of Working Group III to the Sixth Assessment Report of the Intergovernmental Panel on Climate Change [P.R. Shukla, J. Skea, R. Slade, A. Al Khourdajie, R. van Diemen, D. McCollum, M. Pathak, S. Some, P. Vyas, R. Fradera, M. Belkacemi, A. Hasija, G. Lisboa, S. Luz, J. Malley, (eds.)]. Cambridge University Press, Cambridge, UK and New York, NY, USA. doi: 10.1017/9781009157926

[5] Retrieved from :" https://www.graphicnews.com/en/pages/42154/energy-europes-dependency-on-russian-gas"

[6] European Commission, www.consilium.europa.eu/en/policies/green-deal/fit-for-55-the-eu-plan-for-a-green-transition/, 2021

[7] European commission, Communication from the commission to the European parliament, the European council, the council, the European economic and social committee, and the committee of the regions, REPowerEU Plan, 2022

[8] EU Commission staff, Implementing the repower EU action plan: investment needs, hydrogen accelerator and achieving the bio-methane targets, REPowerEU Plan, 2022

[9] Furat Dawood, Hydrogen production for energy: An overview, International Journal of Hydrogen energy, 45, 3847-3869, 2020

[10] A.G. Olabi, Adel saleh bahri, Large-scale hydrogen production and storage technologies: Current status and future directions, International Journal of Hydrogen Energy, 46, 23498-23528, 2021

[11] R.S. El-Emam, H. Ozcan, Comprehensive review on the techno-economics of sustainable large-scale clean hydrogen production, Journal of Cleaner Production, 220, 593-609, 2019.

[12] Marco Martino, Concetta Ruocco, Main Hydrogen Production Processes: An Overview, Catalysts, 11, 547, 2021.

[13] Haris Ishaq, A review on hydrogen production and utilization: Challenges and opportunities, International Journal of Hydrogen Energy, 47, 26238-26264, 2022

[14] Hannah Ritchie, Max Roser and Pablo Rosado (2022) - "Energy". Published online at OurWorldInData.org. Retrieved from: 'https://ourworldindata.org/energy'

[15] Massimo Moser, Matteo Pecchi, Techno-Economic Assessment of Solar Hydrogen Production by Means of Thermo-Chemical Cycles, Energies, 12, 2019, 352

[16] Rengui Li, Latest progress in hydrogen production from solar water splitting via photocatalysis, photoelectrochemical, and photovoltaic-photoelectrochemical solutions, Chinese Journal of Catalysis, 38, 5-12, 2017

[17] Alexander Samokhvalov, Hydrogen by photocatalysis with nitrogen codoped titanium dioxide, Renewable and Sustainable Energy Reviews, 72, 981-1000, 2017

[18] Neda Akhlaghi, Ghasem Najafpour-Darzi, A comprehensive review on biological hydrogen production, International Journal of Hydrogen energy, 45, 22492-22512, 2020

[19] Ye Wu, Michael Q. Wang, Anant D. Vyas, David C. Wade & Temitope A. Taiwo, Well-to-Wheels Analysis of Energy Use and Greenhouse Gas Emissions of Hydrogen Produced with Nuclear Energy, Nuclear Technology, 155:2, 192-207, DOI: 10.13182/NT06-A3756, 2006

[20] Ibrahim Dincer, M. Tolga Balta, Potential thermochemical and hybrid cycles for nuclear-based hydrogen production, Int. J. Energy Res, 35, 123-137, 2011

[21] Mahsa Kheirollahivash, et al., Plasma Chemistry and Plasma Processing, 39, 445, 2019

[22] Yuan Gao, et al., Applied Energy, 226, 534–545, 2018

[23] Omid Khalifeh, et al., Applied Energy, 169, 585, 2016

[24] Hao Zhang, et al., International journal of hydrogen energy, 39, 1260,2014

[25] J. Mizeraczyk, et al., 2014

[26] Angjian Wu, et al., Applied Energy, 195, 67, 2017

[27] Faisal Saleem, et al., Chemical Engineering & Processing: Process Intensification, 142, 107557, 2019

[28] Alan Maslani, et al., international journal of hydrogen energy, 46, 1605, 2021

[29] R Fincke, Plasma Pyrolysis of Methane to Hydrogen and Carbon Black, Ind. Eng. Chem., 41, 1425-1435, 2002

[30] Jing Xia Qian, et al., Journal of Cleaner Production, 320, 128879, 2021

[31] Ahmed E. Awadallah, et al., Journal of Environmental Chemical Engineering, 9 ,106023 , 2021

[32] Juliana Alves Silva, et al., International journal of hydrogen energy, 2021

[33] G. Gomez-Pozuelo, et al., Fuel, 306, 121697, 2021

[34] Rahul Kundu ,et al. , Energy Fuels, 35, 13523, 2021

[35] Muhammad Anees Ul Hasnain ,et al. , International journal of hydrogen energy, 2021

[36] M. Steenbeck, Z. Phys. 33, 809, 1932.

[37] Y. P. Raizer, Teplofiz. Vys. Temp. 10, 1152, 1974.

[38] Y. P. Raizer, Gas Discharge Physics, Springer, 1991.

[39] A. Fridmann, Plasma Chemistry, Cambridge University Press, 194-197, 2008

[40] Cuoci, A., Frassoldati, A., Faravelli, T., Ranzi E., OpenSMOKE++: An object-oriented frame-work for the numerical modeling of reactive systems with detailed kinetic mechanisms, Computer Physics Communications, 192, p. 237-264 (2015), DOI: 10.1016/j.cpc.2015.02.014

[41] Cuoci, A., Frassoldati, A., Faravelli, T., Ranzi, E., Numerical Modeling of Laminar Flames with Detailed Kinetics Based on the Operator-Splitting Method, Energy and Fuels, 27 (12), pp. 7730-7753 (2013), DOI: 10.1021/ef4016334

[42] P.J. Linstrom and W.G. Mallard, Eds., NIST Chemistry WebBook, NIST Standard Reference Database Number 69, National Institute of Standards and Technology, Gaithersburg MD, 20899, https://doi.org/10.18434/T4D303, (retrieved February 24, 2022).

[43] S. A. Khrapak, On the conductivity of moderately non-ideal completely ionized plasma, Results in physics, 17, 2020

List of Figures

Figure 1.0.1: Global GHG Emissions and warming scenarios. Source: Our World in Data [3]. 1

Figure 1.0.2: European countries dependance on gas from the Russian Federation. Source Eurostat, Bloomberg, and Statista [5]..... 2

Figure 1.0.3: Three main programmatic points of REPowerEU plan [7]. 3

Figure 1.0.4: Hydrogen use by sector in 2030 (Mt H2); Source: Modelling using PRIMES [7]..... 4

Figure 1.1.1: Routes for sustainable clean hydrogen production. [11]..... 7

Figure 1.1.2: Cost range of hydrogen production technologies based on energy source. [11] 8

Figure 1.1.3: Hydrogen production cost by renewable and non-renewable energies in 2019 [10] 8

Figure 1.1.4: Scheme of hydrogen production by electrolyser [10] 11

Figure 1.1.5: Solar power generation, 2021, electricity generation from solar, measured in TWh per year. Source: Our World in Data [14]..... 11

Figure 1.1.6: Two stages of the water-splitting process [15]..... 12

Figure 1.1.7: Hydrogen production by solar PV system. [10] 13

Figure 1.1.8: Three different configurations for PEC water splitting system are explored, single photoanode, single photo-cathode, photoanode and photocathode tandem system. [16]..... 14

Figure 1.1.9: New valence band formation by doping of nonmetal ions. [17]..... 15

Figure 1.1.10: Wind power generation, 2021, Annual electricity generation from wind is measured in TWh per year Source: Our World in Data [14]..... 16

Figure 1.1.11: Onshore and offshore wind energy-driven hydrogen production. [12] 17

Figure 1.1.12: Hydrogen production schematic using biomass thermochemical conversion: gasification and pyrolysis. [10]..... 18

Figure 1.1.13: Three examples of the taxonomic composition of H2-producing communities dominated [12] 19

Figure 1.1.14: Direct and indirect bio photolysis processes of photosynthetic microorganisms [12] 20

Figure 1.1.15: Nuclear power generation, 2021, Source: Our World in Data [14] ... 21

Figure 1.1.16: Four principal production strategy of hydrogen using nuclear reactors [19] 22

Figure 1.2.1: Mobile and Elongating Arc Plasma Reactor. [21] 24

Figure 1.2.2: Settings of microsecond pulsed spark reactor. [22] 25

Figure 1.2.3: Schematic diagram of nanosecond pulsed DBD setup. [23] 25

Figure 1.2.4: Configuration of the RGA discharge reactor. [24] 26

Figure 1.2.5: Configuration of a waveguide-supplied metal-cylinder-based microwave plasma reactor. [25] 26

Figure 1.2.6: Configuration of PlasGas reactor. [28] 27

Figure 1.2.7: Schematic of torch, injector, and reactor; flow is left to right. [29] 27

Figure 2.3.1: Structure of OpenSMOKE++ suite. [40, 41] 46

Figure 3.1.1: Electric conductivity of the arc in methane plasma as a function of average temperature in the discharge. 52

Figure 3.1.2: Electric field of the methane plasma arc as a function of the average temperature in the discharge. 53

Figure 3.1.3: Radius of methane plasma arc column as a function of the average temperature in the discharge. 53

Figure 3.1.4: Discharge power per unit length of methane plasma arc as a function of the average temperature in the discharge. 54

Figure 3.1.5: Average plasma temperature as a function of the chamber radius R 60

Figure 3.1.6: Average plasma temperature as a function of the chamber radius R 60

Figure 3.3.1 : Molar fraction at equilibrium conditions at 0.1 bar and in the 1500-3000 °C temperature range. 63

Figure 3.3.2: Molar fraction at equilibrium condition at 1 bar and in the 1500-3000 °C temperature range. 64

Figure 3.3.3. Molar fraction at equilibrium condition at 10 bar and in the 1500-3000 °C temperature range. 64

Figure 3.3.4: Molar fraction at equilibrium condition at 100 bar and in the 1500-3000 °C temperature range. 65

Figure 3.3.5: Molar fraction at equilibrium condition at 1 bar and in the 3000-6000 °C temperature range. 66

Figure 3.3.6: Molar fraction at equilibrium condition at 1 bar and in the 6000-10000 °C temperature range. 66

Figure 3.3.7: Molar fraction at equilibrium condition at 1 bar and in the 10000-15000 °C temperature range. 67

Figure 3.3.8: Molar fraction at equilibrium condition at 1 bar and in the 15000-20000 °C temperature range. 68

Figure 3.3.9: Equilibrium of a 1 mol of methane at 0.1 bar and in the 0-6000 °C temperature range. 69

Figure 3.3.10: Equilibrium of a 1 mol of methane at 1 bar and in the 0-6000 °C temperature range. 70

Figure 3.3.11: Equilibrium of a 1 mol of methane at 10 bar and in the 0-6000 °C temperature range. 70

Figure 3.3.12: Equilibrium of a 1 mol of methane at 50 bar and in the 0-6000 °C temperature range. 71

Figure 3.3.13: Equilibrium of a 1 mol of methane at 100 bar and in the 0-6000 °C temperature range. 71

Figure 3.3.14: Equilibrium of a 1 mol of methane in a diluted system with Argon, whose molar fraction is 0.5, at 1 bar and in the 0-6000 °C temperature range. 72

Figure 3.3.15: Equilibrium of a 1 mol of methane in a diluted system with Argon, whose molar fraction is 0.9, at 1 bar and in the 0-6000 °C temperature range. 73

Figure 3.3.16: Equilibrium of a 1 mol of methane in a diluted system with Argon, whose molar fraction is 0.99, at 1 bar and in the 0-6000 °C temperature range. 73

Figure 3.4.1: Hydrogen molar fraction profile at different conditions based on second Fincke experiment inlet data. 77

Figure 3.4.2: Temperature profile at different conditions based on first Fincke experiment inlet data. 80

Figure 3.4.3: Hydrogen molar fraction profile at different conditions based on second Fincke experiment inlet data. 81

List of Tables

Table 1.1: Non-Thermal Plasma Specific Energy Requirement (SER) 28

Table 1.2: Thermal plasma Specific Energy Requirement (SER) 29

Table 1.3: Catalytic decomposition of methane (CDM) Specific Energy Requirement (SER) (if available) and other important data..... 30

Table 2.1: Properties of Heavy PAHs 48

Table 2.2: Properties of Soot Particles..... 48

Table 2.3: Properties of Soot Aggregates..... 49

Table 3.1: Operating parameters of the case study. 54

Table 3.2: Operating parameters of the case study. 55

Table 3.3: First case about the variation of operating parameters in the plasma column. 56

Table 3.4: Second case about the variation of operating parameters in the plasma column. 56

Table 3.5: Third case about the variation of operating parameters in the plasma column. 57

Table 3.6: Methane arc plasma properties as a function of the chamber radius R.. 58

Table 3.7: Data of an alternative model for the plasma discharge. 61

Table 3.8: Results of an alternative model for the plasma discharge. 61

Table 3.9: Results comparison of the two different model. 62

Table 3.10: Inlet conditions of the first experimental setup considered [29]. 75

Table 3.11: Inlet conditions of the first experimental setup considered [29]. 75

Table 3.12: Results from simulations of first Fincke setup with a final temperature of 300 K..... 78

Table 3.13: Results from simulations of first Fincke setup with a final temperature of 800 K..... 78

Table 3.14: Results from simulations of first Fincke setup with a final temperature of 1300 K. 79

Table 3.15: Results from simulations of second experimental setup with a final temperature of 300 K. 82

Table 3.16: Results from simulations of second experimental setup with a final temperature of 800 K. 82

Table 3.17: Results from simulations of second experimental setup with a final temperature of 1300 K. 82

Acknowledgments

First, I want to thank Professor Carlo Alessandro Cavallotti, who made this work possible and always encouraged me through precious advices.

I am grateful to my friends that were always there when needed, for their incredible tenacity, that were a light in the darkest times. They have always been best of me.

Finally, the most special thanks go to my family, specially to my parents and my sister Veronica, for the support throughout all these years. This accomplishment would not have been possible without you.